

ACCEPTED MANUSCRIPT • OPEN ACCESS

Recent advances in acoustic diagnostics for electrochemical power systems

To cite this article before publication: Jude Majasan *et al* 2021 *J. Phys. Energy* in press <https://doi.org/10.1088/2515-7655/abfb4a>

Manuscript version: Accepted Manuscript

Accepted Manuscript is “the version of the article accepted for publication including all changes made as a result of the peer review process, and which may also include the addition to the article by IOP Publishing of a header, an article ID, a cover sheet and/or an ‘Accepted Manuscript’ watermark, but excluding any other editing, typesetting or other changes made by IOP Publishing and/or its licensors”

This Accepted Manuscript is © 2021 The Author(s). Published by IOP Publishing Ltd.

As the Version of Record of this article is going to be / has been published on a gold open access basis under a CC BY 3.0 licence, this Accepted Manuscript is available for reuse under a CC BY 3.0 licence immediately.

Everyone is permitted to use all or part of the original content in this article, provided that they adhere to all the terms of the licence <https://creativecommons.org/licenses/by/3.0>

Although reasonable endeavours have been taken to obtain all necessary permissions from third parties to include their copyrighted content within this article, their full citation and copyright line may not be present in this Accepted Manuscript version. Before using any content from this article, please refer to the Version of Record on IOPscience once published for full citation and copyright details, as permissions may be required. All third party content is fully copyright protected and is not published on a gold open access basis under a CC BY licence, unless that is specifically stated in the figure caption in the Version of Record.

View the [article online](#) for updates and enhancements.

Recent Advances in Acoustic Diagnostics for Electrochemical Power Systems

Jude O. Majasan^a, James B. Robinson^{a,b,*}, Rhodri E. Owen^{a,b}, Maximilian Maier^a, Anand N. P. Radhakrishnan^a, Martin Pham^a, Thomas G. Tranter^{a,b}, Yeshui Zhang^{a,b}, Paul R. Shearing^{a,b} and Dan J. L. Brett^{a,b,*}

^a*Electrochemical Innovation Lab, Department of Chemical Engineering, UCL, London, WC1E 7JE, UK*

^b*The Faraday Institution, Quad One, Harwell Science and Innovation Campus, Didcot, OX11 0RA, UK*

* Corresponding authors: j.b.robinson@ucl.ac.uk; d.brett@ucl.ac.uk

Abstract

Over the last decade, acoustic methods, including acoustic emission and ultrasonic testing, have been increasingly deployed for process diagnostics and health monitoring of electrochemical power devices, including batteries, fuel cells, and water electrolysers. These techniques are non-invasive, highly sensitive, and low-cost, providing a high level of spatial and temporal resolution and practicality. Their application in electrochemical devices is based on identifying changes in acoustic signals emitted from or propagated through materials as a result of physical, structural, and electrochemical changes within the material. These changes in acoustic signal are then correlated to critical processes and the health status of these devices. This review summarizes progress in the use of acoustic methods for the process and health-monitoring of major electrochemical energy conversion and storage devices. First, the fundamental principles of acoustic emission and ultrasonic testing are introduced, then the application of these acoustic techniques to the electrochemical power devices are discussed. Conclusions and perspectives on some of the key challenges and potential commercial and academic applications of the devices are highlighted. It is expected that, with further developments, acoustic techniques will form a key part of the suite of diagnostic techniques routinely used to monitor electrochemical devices across various processes, including fabrication, post-mortem examination and recycle decision support to aid the deployment of these devices in increasingly demanding applications.

Keywords:

Acoustic Emission; Ultrasonic Testing; Li-ion battery; fuel cells; water electrolyser; acoustic time-of-flight; amplitude.

32 1.0 Introduction

33 In the last few decades, extensive attention has been paid to weaning global energy production away from
34 fossil fuels to address environmental sustainability and energy security concerns. This is evidenced by the
35 increasing adoption of renewable energy sources (solar, wind, and tidal), with penetration projected to
36 exceed 25% by 2030 [1]. Alongside this, global energy demands have substantially increased due to
37 population growth, rapid industrialisation and urbanisation, particularly in the developing and emerging
38 economies [2,3]. This combination of factors is driving the demand for highly efficient, scalable and
39 economical technologies for energy production and storage with electrochemical devices including
40 batteries, fuel cells, supercapacitors and electrolyser technologies delivering solutions and showing great
41 promise [4]. These devices are well placed to form a significant component of a future, low-carbon energy
42 market, facilitating the use of intermittent, renewable energy sources in sectors as diverse as grid-scale
43 electricity distribution, transportation and portable consumer electronics [5–7].

44
45 Some of the most promising electrochemical energy conversion devices include lithium-ion batteries (LIBs)
46 [8,9], redox flow batteries (RFBs) [10,11], polymer electrolyte membrane fuel cells (PEMFCs) [12,13],
47 solid oxide fuel cells (SOFCs) [14] and polymer electrolyte membrane water electrolysers (PEMWEs)
48 [2,15]. Each of these devices possesses unique benefits which favour different energy conversion and
49 storage applications. LIBs, for instance, are among the most widely used rechargeable batteries having
50 advantages, including a high voltage, long cycling life, and low self-discharge [16]. RFBs offer a relatively
51 cheap energy storage solution with high energy efficiency, long cycle life, minimal safety issues and high
52 scale-up flexibility [17]. Fuel cells offer a bridge between electric power generation and chemical energy
53 storage and provide unique advantages in heavy-duty and long-range automotive applications [18–22].
54 PEMFC, in particular, offers benefits including high energy density, modular design, low noise and
55 vibrations, easy installation and compatibility with dynamic load profiles [13,18]. SOFC has advantages
56 such as high energy conversion efficiency, all-solid-state structure, increased fuel flexibility and robustness
57 to catalytic poisoning alongside the prospect of deployment in combined heat and power scenarios due to
58 the high-quality exhaust heat and high power density [23,24]. Similarly, in water electrolysis, PEMWE
59 offers a high current density of operation, compactness and ease of integration with renewable energy
60 sources, crucial to the prospect of a renewable hydrogen economy [15,25]. Taken together, this portfolio of
61 devices are well suited for integration into energy production for domestic, industrial, automotive and
62 consumer electronics applications.

63
64 To maximise the potential of these devices, further improvements are required to address performance,
65 durability, and cost issues. For instance, current demands on LIBs include higher power and energy density

1
2
3 66 and extending the operating cycling life of cells for first-life applications [16]. Additionally, due to the
4 67 increased uptake of battery electric vehicles (BEVs) and hybrid-electric vehicles (HEVs) in which batteries
5 68 are deployed as a high-value component, significant improvement is sought for the *operando* prediction of
6 69 the state of health (SoH) and degradation [26,27]. In RFBs, more accurate state of charge (SoC) estimation
7 70 is of vital importance for better operational safety and performance as extremes of SoC both degrades the
8 71 system and causes dangerous gas formation [28]. In PEMFCs, a better understanding of degradation and
9 72 water management is crucial to improve efficiency, reliability and durability for a broad range of
10 73 applications [29–32]. In SOFCs, improving reliability and durability is contingent on improved mechanical
11 74 properties related to thermal stresses induced by temperature gradients or differences in thermal expansion
12 75 of components [33]. Also, wider deployment of PEMWEs depends on higher current density operation,
13 76 which requires an improved understanding of mass transport alongside optimised component designs
14 77 necessary for improved efficiency and cell performance [34,35].
15
16
17
18
19
20
21
22
23

24 79 To aid development in these areas, several ex-situ and in-situ diagnostic techniques have been widely
25 80 deployed for the fabrication, design, performance assessment and monitoring of electrochemical devices
26 81 [15,27,36–41]. These range of techniques includes electrochemical, physical and optical spectroscopic
27 82 tools and X-ray scattering, spectroscopy, and tomography techniques [42–45], AC impedance and
28 83 voltammetry [46], transmission electron microscopy [47,48], nuclear magnetic resonance [49], atomic force
29 84 microscopy [50], and neutron [51] and optical imaging [52,53]. Although these tools have collectively
30 85 provided rich data for design and performance analysis of the various electrochemical power devices, they
31 86 also have important limitations.
32
33
34
35
36
37

38 88 Recently, acoustic methods have emerged as a simple, low cost, and non-invasive tool with huge promise
39 89 for *in-situ* and *operando* monitoring of the chemical, mechanical and structural processes in electrochemical
40 90 power devices. The acoustic methods are divided into two primary forms, both of which are explored in
41 91 this review. First, the acoustic emission (AE) technique, a passive monitoring tool which detects acoustic
42 92 events generated within a material or device. The acoustic events occur spontaneously when the material
43 93 or device is subjected to stress and typically arise from a physical change within the system such as crack
44 94 generation, corrosion, oxide formation, gas evolution, electrode deformation or fluid motion (two-phase
45 95 flow) [54]. The AE technique is not impacted by the nature of the stress and is therefore powerful for failure
46 96 or degradation detection within a system. The ultrasonic testing (UT) technique, on the other hand, is an
47 97 active technique in which externally generated acoustic signal is introduced and propagated through the
48 98 material to study the internal structure and processes. This technique enables the interrogation of the
49 99 condition of the system as acoustic wave propagation depends on an array of factors discussed later in this
50
51
52
53
54
55
56
57
58
59
60

1
2
3 100 work. The fundamental distinction between these two acoustic forms is that the AE technique monitors the
4 101 emission originating from the test material itself, whereas the UT uses an externally generated signal to
5 102 monitor the material response. That is, AE “listens” for the energy released by the material or device,
6 103 whereas UT actively probes the test material by supplying energy to it and monitoring the response [54].
7
8
9
10

11 105 This review first provides a brief description of the principle underlying each of the two basic forms,
12 106 thereafter recent progress in the application of acoustic techniques to electrochemical power systems is
13 107 highlighted. Finally, some of the key challenges of applying acoustic diagnostics to the various technologies
14 108 are discussed, and promising future research directions and application areas are identified.
15
16
17
18

19 109 **2.0 Principle and Practice of Acoustic Methods**

20 21 22 110 **2.1 Acoustic Emission**

23 111 Acoustic emission (AE) is a passive non-destructive technique whereby transient elastic waves are
24 112 generated by the rapid release of energy from a localised source or sources within a solid material [55].
25 113 Under an external stimulus (for instance, change in pressure, strain, temperature or load), localised sources
26 114 within the material trigger the release of energy in the form of stress waves ranging from audible (a few
27 115 hertz) to ultrasonic frequencies in the megahertz range. These stress waves propagate to the surface and can
28 116 be detected and converted to electrical signals using piezoelectric sensors [54,56]. Acoustic emissions can
29 117 be detected at frequency ranges below 1 kHz and up to 100 MHz, although typically within the 1 kHz to 1
30 118 MHz range. With suitable equipment, vibrational displacement on the scale of picometers (10^{-12} m) can be
31 119 detected in components [57].
32
33
34
35
36
37
38

39 121 There are four main modes of acoustic wave propagation, these are longitudinal (or compressional wave),
40 122 transverse (or shear waves), Rayleigh waves (or surface waves), and Lamb waves (or plate waves) [58].
41 123 Acoustic waves are generally classified as body (or bulk) waves and surface (or guided) waves.
42 124 Longitudinal and transverse waves are body waves because they propagate through the bulk material.
43 125 Rayleigh waves and Lamb waves are surface or guided waves because they are propagated along the
44 126 material surface and ‘guided’ by the geometric boundary of the material. When considering longitudinal
45 127 waves, the vibration occurs in the direction of wave propagation, whereas transverse waves involve the
46 128 vibration of particles at right angles to the direction of wave propagation. Rayleigh waves travel on the free-
47 129 boundary (surface) of elastic solids. They combine both longitudinal and transverse motion into elliptic
48 130 vibrations whose energy decays exponentially as the distance from the surface increases. Lamb waves are
49 131 guided waves in thin plates (thickness of the order of magnitude of the acoustic wavelength) created by
50
51
52
53
54
55
56
57
58
59
60

1
2
3 132 coupling between longitudinal and transverse waves reflected at the top and the bottom of the plate. Lamb
4 133 waves can move the entire thickness of the plate and are dispersive due to being guided by the faces of the
5 134 plates, and their propagation occurs in both symmetric and asymmetric modes [59].
6
7

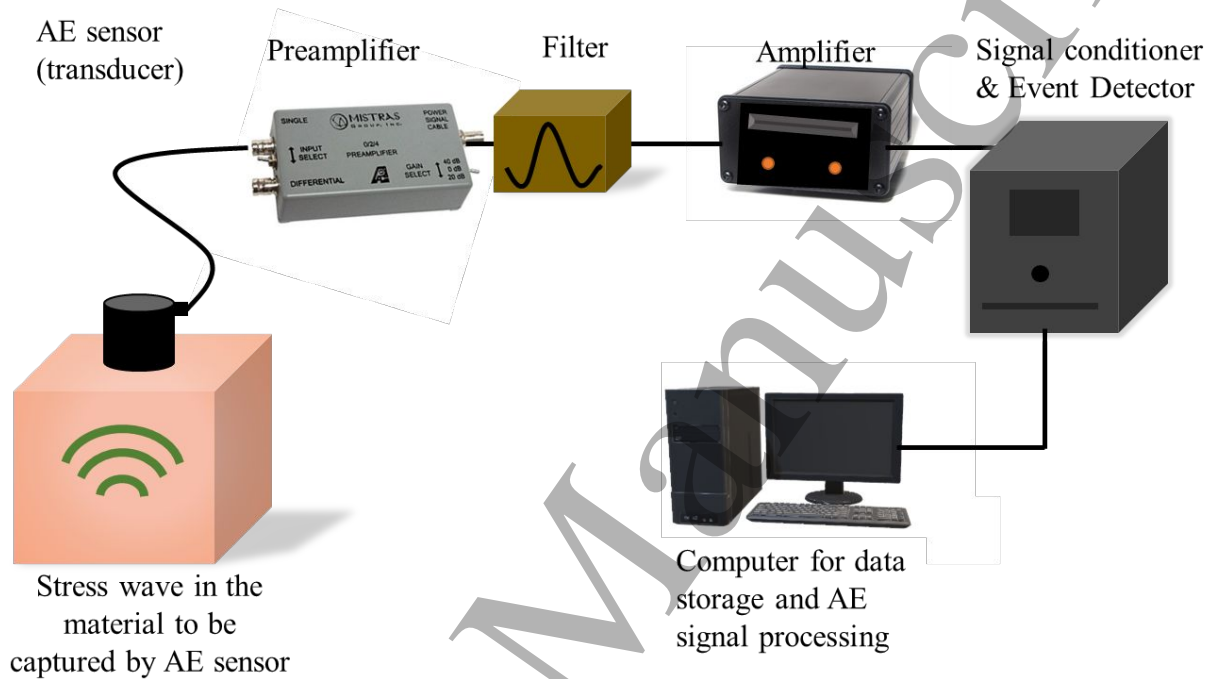
8 135
9 136 AE has been widely used since the 1960s to detect anomalies such as leakages and cracks on large
10 137 structures, including bridges, pressure containers, and pipelines transporting liquids under high pressure
11 138 [60]. The technique is now being employed in many research and industrial applications as a powerful non-
12 139 destructive evaluation tool for dynamic safety monitoring, early damage warning, and failure prevention of
13 140 mechanical equipment and structures [61,62]. AE signals have been used to characterise degradation
14 141 mechanisms of various materials under chemical, mechanical or thermal stresses and have been used for
15 142 diagnostics of a wide range of electrochemical phenomena, including anodisation [63,64], corrosion
16 143 [3,65] and oxygen reduction [66].
17
18
19
20
21
22

23 144 **2.1.1 Instrumentation**

24 145 A typical AE monitoring setup is shown in Figure 1, consisting of a sensor, preamplifier, filter, amplifier,
25 146 alongside data acquisition and signal processing units. The microscopic mechanical perturbation caused by
26 147 an AE event is captured by sensors mounted on the surface of the material, which converts the mechanical
27 148 vibrations into an electrical signal. Piezoelectric sensors, specifically lead–zirconate–titanate (PZT)
28 149 transducers, are often used as electromechanical conversion devices as they provide a good combination of
29 150 sensitivity, signal-to-noise ratio and dynamic range [67]. Alternative transduction methods, such as fibre
30 151 optic sensors, have also been demonstrated in recent times and may find use in speciality applications [68–
31 152 70]. Couplant, typically moderately viscous, nontoxic liquids, gels, or pastes such as silicone grease, is
32 153 usually necessary to provide sufficient acoustic contact between the sensor and the surface of the test object.
33 154 The signal obtained at the sensor output often has low amplitude, requiring significant amplifications for
34 155 ease of processing. Typical amplification gains in the order of 40-100 dB provide an optimal balance
35 156 between events monitoring and noise exclusion [59]. Amplification is generally performed in two stages.
36 157 Preamplifiers perform a first amplification and a low impedance matching of the acoustic signal. The
37 158 preamplifier is often placed close to the transducer to minimise interference, with many current transducers
38 159 having an integrated preamplification. Following preamplification, the signal is relayed to a bandpass or
39 160 high-pass filters to eliminate low frequencies (background noise) and very high frequencies outside the
40 161 practical frequency range of about 20 kHz to 1 MHz. The lower frequency limit is governed by background
41 162 noise, and consequently, is rarely reduced below 10–20 kHz, whereas the upper-frequency limit is governed
42 163 by wave attenuation, which is particularly significant in composite materials, and rarely exceeds 1 MHz
43 164 [67]. The second amplification brings the signal to a sufficient amplitude for subsequent processing. The
44
45
46
47
48
49
50
51
52
53
54
55
56
57
58
59
60

165 signal conditioning circuits then convert the analogue signal to a digital form, then the acquired signal can
 166 be analysed and stored using computer software. Each mechanical phenomenon, i.e. source of an acoustic
 167 event, within the material leads to a transient acoustic wave which is then classified and analysed using
 168 several acoustic parameters.

169



170

171

172 **Figure 1 Schematic of the hardware used in the acquisition of a typical acoustic emission signal.**

173 2.1.2 Acoustic Emission Parameters

174 Figure 2 shows a typical AE waveform and the most common acoustic signal descriptors. Various factors
 175 contribute to the shape of the AE waveform, including the characteristics of the AE source, the wave
 176 propagation behaviour (e.g. wave modes, velocity, reflection, attenuation, and interference) and the AE
 177 sensor response. As acoustic waves propagate through the material of interest, the amplitude is reduced due
 178 to signal attenuation, which occurs through several basic mechanisms, including signal absorption,
 179 scattering, dispersion and beam spreading (divergence or geometric attenuation) [67].

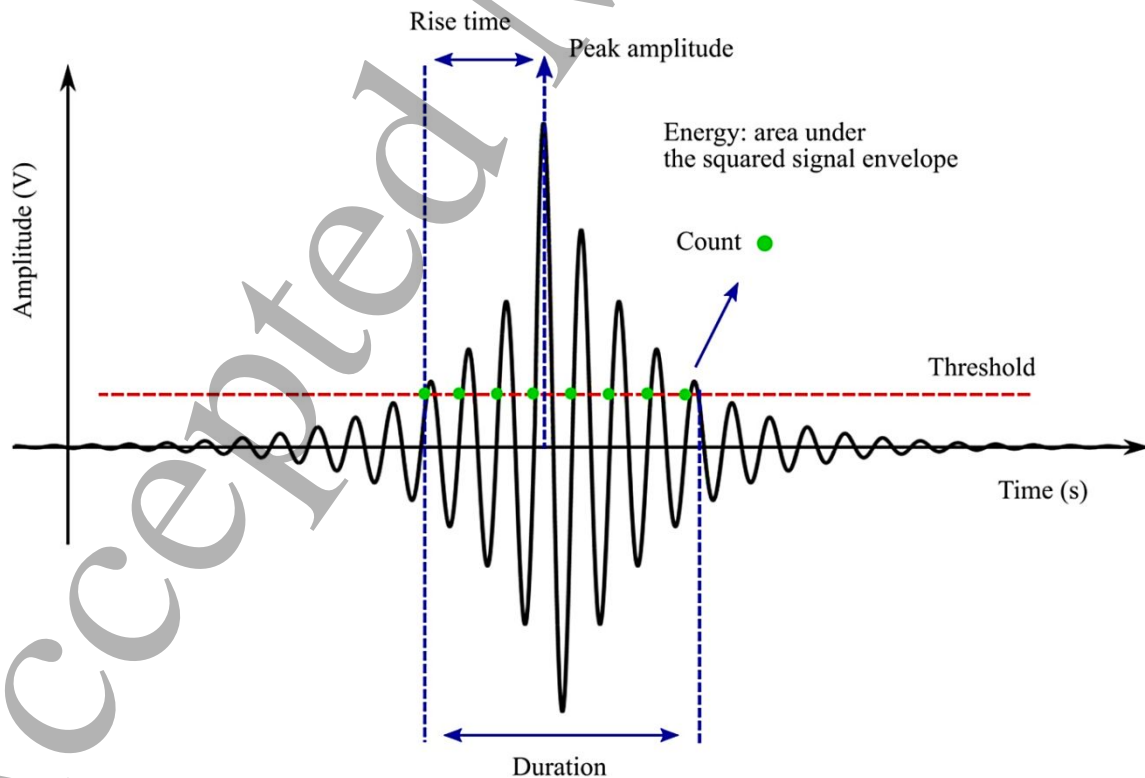
180

181 In AE testing, a threshold level of waveform amplitude is often set to reduce noise interference and improve
 182 the signal-to-noise ratio. Once this has been performed, only acoustic events that exceed this predefined
 183 threshold are taken into account. The subsequent waveform obtained can be described through an
 184 understanding of several key parameters. The amplitude of the signal, one of the most informative signal

185 descriptor, is described by the maximum (positive or negative waveform) AE signal excursion during an
 186 AE hit, expressed in decibels (dB). A typical AE signal (waveform) is represented as a voltage versus time
 187 curve, for which the voltage is converted to dB using Equation (1), where A is the amplitude (dB), V_{sig} is
 188 the voltage of the measured signal and V_{ref} is the reference voltage, typically 1 μV . Generally, the decibel
 189 scale runs from 0 dB (100 μV) to 100 dB (10V) [71].

$$A = 20 \log \frac{V_{sig}}{V_{ref}} \quad (1)$$

191 Further important descriptors include the rise time, i.e. the time between the first threshold crossing and the
 192 peak amplitude, the ‘duration’ or the time interval between first and last threshold crossing in the burst
 193 signal, ‘counts’ or the number of occasions that the waveform crosses the threshold in the increasing
 194 direction within the duration, and the energy of an event, typically in the order of attoJoules (1 aJ = 10^{-18}J),
 195 defined as the integral of the square of the signal voltage over its duration. The peak frequency (Hz),
 196 corresponding to the highest magnitude in the frequency distribution obtained by methods such as from
 197 Fast Fourier transform (FFT) of the signal can also be used to describe acoustic events [54]. Acoustic events
 198 are often released discontinuously in time; thus, another common representation is a plot of the cumulated
 199 number of ‘hits’ or the cumulated absolute energy (CAEE) against the time over which measurements were
 200 made. A high-gradient curve indicates periods of high acoustic activity, while a plateau indicates periods
 201 of low acoustic activity.



1
2
3 203 **Figure 2 A typical acoustic emission signal obtained from a sample with the primary characteristics of the peaks including**
4 204 **the rise time, peak amplitude and count described[72].**

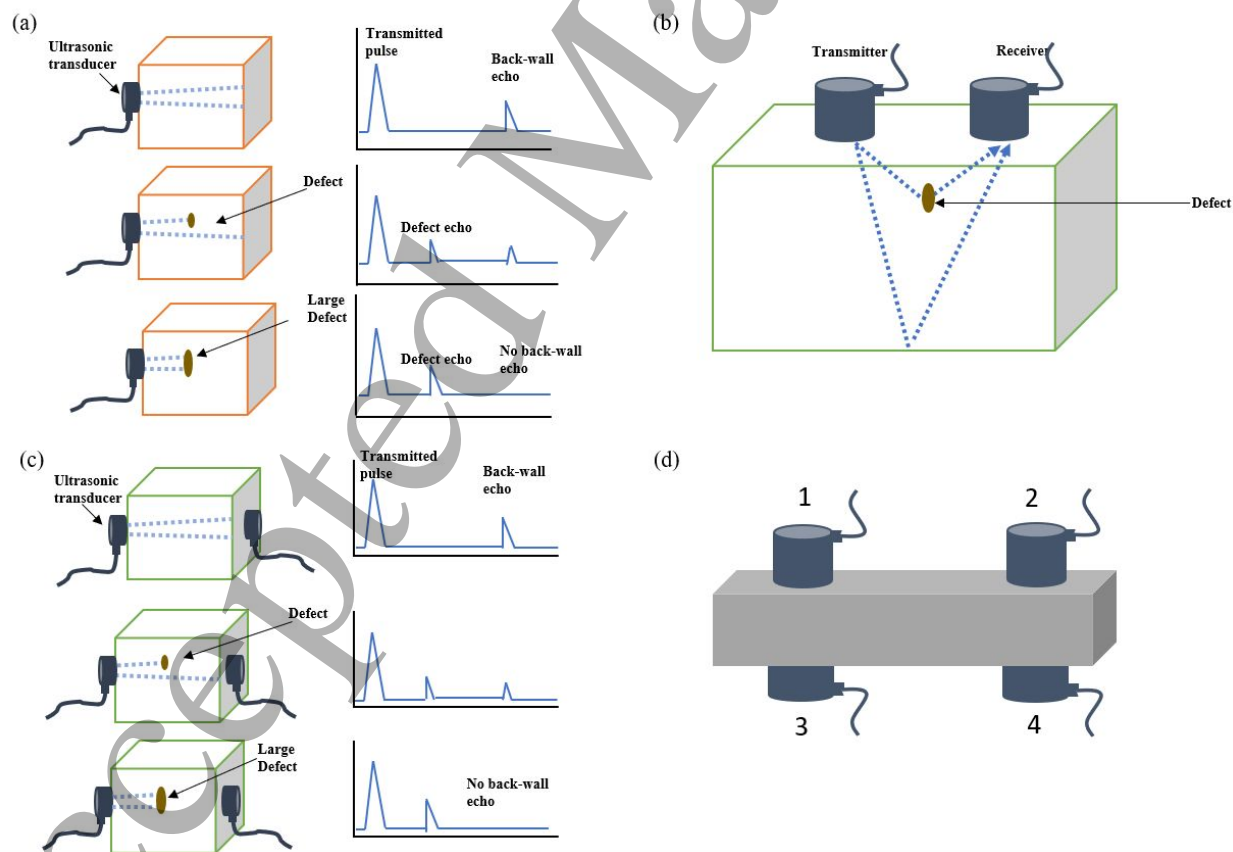
7 205 **2.2. Ultrasonic Testing**

9 206 The ultrasonic testing (UT) technique is based on the principle that high-frequency sound wave will travel
10 207 through a given medium at a specific velocity, in a predictable direction, until they encounter a boundary
11 208 with a different medium, where they will be reflected or transmitted. Thus, when ultrasonic waves
12 209 encounter cracks, phase interface, voids or other discontinuities in a test object, a portion of the sound waves
13 210 is reflected, and the remainder is transmitted, allowing real-time monitoring of material properties, internal
14 211 damage, and structural integrity. UT is often performed at frequencies well above the audible range,
15 212 typically in the megacycle range between 0.5 and 25 MHz [73].
16
17
18
19
20

21 213
22 214 As in AE, the transducer probe contains a piezoelectric crystal that generates ultrasonic pulses propagated
23 215 into the test object. The main modes of the ultrasonic inspection may be classed into three: pulse-echo,
24 216 pitch-catch, and through-transmission modes [74], and these basic configurations have been applied in
25 217 various forms. Pulse-echo mode involves the use of single-element or multi-element sensors, which act first
26 218 as emitters of ultrasonic pulses and then as receivers to detect echoes from defects or other discontinuities.
27
28 219 Dual-element probes with separate transducers mounted in the same holder for transmission and reception
29 220 have also been used. This configuration eliminates noise in the reflected pulse by avoiding overlap in
30 221 oscillation from the generated ultrasonic pulse. Also, because pulse-echo detects the reflected waves, more
31 222 structural information about the test material interfaces can be attained. The pulse-echo arrangement is
32 223 illustrated in Figure 3(a) for the case of no defect, a small defect and a larger defect. The pitch-catch
33 224 configuration illustrated in Figure 3(b) involves the use of two identical piezoelectric elements, often, but
34 225 not necessarily, mounted in the same holder, with one element serving to emit ultrasonic pulses and the
35 226 other to receive the reflected pulses. In this arrangement, the ultrasonic energy is transmitted at an angle to
36 227 the surface of the test material and received as reflected energy at the reflected angle and is used mainly for
37 228 cylindrical tubes and other nonlinear parallel-sided surfaces. The through-transmission configuration,
38 229 illustrated in Figure 3(c), considered a variation of the pitch-catch mode, involves using two transducers
39 230 located relative to each other on opposite sides of the test material such that one transducer receives the
40 231 energy transmitted from the other after the energy has passed through a region of interest. Transmission
41 232 gives average information about the entire material in the position of the transducer. Most commercial
42 233 transducers are available from below 50 kHz to greater than 200 MHz. Lower frequency provides better
43 234 wave penetration, whereas higher frequency gives better resolution and focal sharpness [74].
44
45
46
47
48
49
50
51
52
53
54

55 235
56
57
58
59
60

236 The ultrasonic display can provide information such as the relative thickness of the material, depth into the
 237 material where flaws or discontinuities are located, and with proper scanning hardware and software, the
 238 location of flaws. A typical waveform display in a simple geometry is shown in Figure 3(a). For the case
 239 of no defects, two pulses are typically displayed, the transmitted pulse and the back-wall echo. The
 240 introduction of a small defect reduces the amplitude of the transmitted pulse and is seen as an intermediate
 241 pulse. A large defect or void can block the transmitted signal, as shown in Figure 3a. For practical
 242 measurement using UT signal (Figure 3d), the arrangement of the probes on the test material is determined
 243 by the mode of wave propagation. For instance, the transmitter and receiver are located on opposite sides
 244 of the test material when the longitudinal mode is used (Sensor 1 and 3). When shear waves are used, the
 245 transmitter and receiver may be located on the same face of the test material (1 and 2) or on the opposite
 246 sides but at opposite ends of the test area (1 and 4 or 2 and 3). When surface waves or Lamb waves are
 247 used, the transducers are located on the same surface but at opposite ends of the test area (Sensor 1 and 2)
 248 [74].



250
 251
 252 **Figure 3 (a) Pulse-echo configuration and simplified screen display for test material without defect, small defect and larger**
 253 **defect. (b) Pitch-catch configuration with sound reflected to the receiver from a defect and back wall. (c) Transmission**

254 configuration and simplified screen display for test material without defect, small defect and larger defect [74]. (d)
255 Placement of transducers in longitudinal, shear, surface or Lamb wave modes.

256 2.2.1 Theory and Implementation

257 A typical ultrasonic testing setup includes an ultrasonic pulser/receiver (transducers), hardware and
258 software for signal capture and analysis, a waveform display and a data logging module. To conduct the
259 test, the piezoelectric transducer sends an ultrasonic pulse through the test object in one of the ultrasonic
260 testing modes: pulse-echo, pitch-catch or through-transmission. As in AE testing, a couplant is necessary
261 to maximise sound energy transfer across the transducer-test material interface. They help minimize the
262 otherwise large acoustic impedance that would arise if the ultrasonic transducer is operated into the air,
263 causing nearly 100% of the ultrasonic energy impinging on air/solid boundaries to be reflected. The three
264 main coupling methods through which the ultrasonic energy is transmitted into the test object include: (1)
265 direct contact between the transducer and the test piece with a liquid or grease couplant between, (2)
266 immersion of the transducer and the test object in a liquid bath and coupling through the intermediate liquid
267 path, and (3) flooding a space separating the transducer and the test piece with a liquid (column or jet) [74].

268
269 The propagation velocity of the wave in a test material depends principally on the density and elastic
270 properties of the material. The general equation for ultrasonic wave velocity for a uniform elastic material
271 is given by Equation (2):

$$272 \quad V_p = \sqrt{\frac{C_{ij}}{\rho}} \quad (2)$$

273 where ρ is the material density, and C_{ij} is the material elastic constant and its directionality with respect to
274 the wave type and direction of travel. Equation 2 may take various forms depending on the mode of wave
275 propagation and the type of elastic constant used. Young's Modulus, E and Poisson's Ratio, σ are the most
276 commonly used elastic constant for determination of propagation velocity of longitudinal waves. For shear
277 waves, the shear modulus, G is commonly used. Thus, the velocity of longitudinal, V_l and shear waves, V_s
278 are described by equations (3) and (4), respectively [75–77]. In practical applications, shear waves travels
279 about half the speed of longitudinal waves.

$$280 \quad V_l = \sqrt{\frac{E(1-\sigma)}{\rho(1+\sigma)(1-2\sigma)}} \quad (3)$$

$$282 \quad V_s = \sqrt{\frac{E}{2\rho(1+\sigma)}} = \sqrt{\frac{G}{\rho}} \quad (4)$$

283

284

At the interface between two dissimilar materials, a portion of the ultrasonic signal is transmitted through the interface, while the rest is reflected. The ratio of reflection to transmission is related to the relative acoustic impedance between the two materials. The bigger the acoustic impedance (Z) mismatch between two layers, the greater the reflection coefficient. The acoustic impedance (Z) of a material, defined as its resistance to the passage of sound energy is calculated as a product of material density (ρ) and ultrasonic velocity V_p .

$$Z = \rho V_p \quad (5)$$

The reflection coefficient R at a planar boundary is calculated as follows:

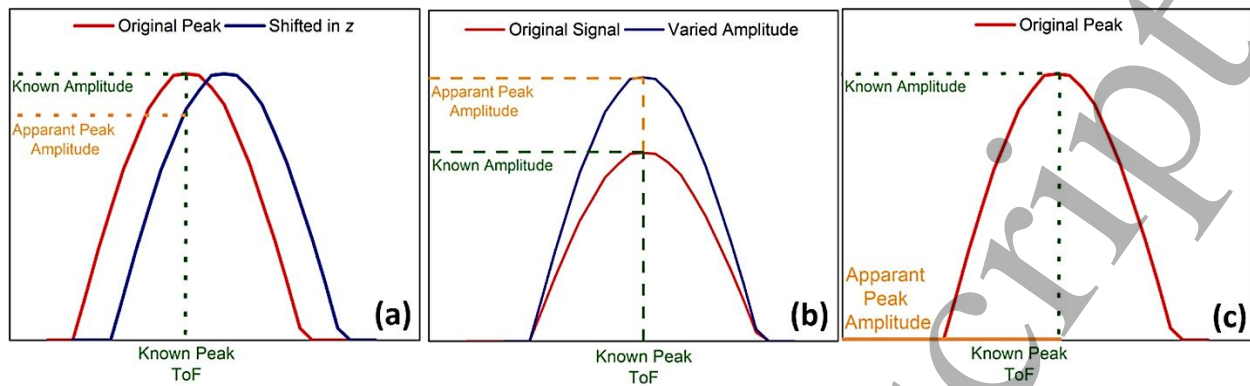
$$R = \left(\frac{Z_2 - Z_1}{Z_2 + Z_1} \right)^2 \quad (6)$$

Where Z_1 is the acoustic impedance of the first medium, and Z_2 is the acoustic impedance of the second medium. From Equation 6, the reflection coefficient decreases as the acoustic impedances of two materials become more similar, whereas dissimilar acoustic impedances leads to a higher reflection coefficient. In theory, the reflection from the boundary between two materials with the same acoustic impedance is zero, whereas, in the case of materials with disparate acoustic impedances, such as the boundary between steel and air, the reflection coefficient approaches 100%.

2.2.2 Ultrasonic Testing Parameters

The two fundamental parameters commonly used for UT analysis are the signal amplitude and the acoustic Time-of-Flight (ToF). The amplitude depicts the size of the reflected signal represented as the height, measured from the lowest to the highest point on a waveform display. Signal amplitude is only a relative measure as it depends on several factors, including the experimental setup, acoustic energy, gain, transducer placement and contact pressure between the transducer and sample. Changes in signal amplitude could occur for a number of reasons, illustrated in Figure 4 [78]. Amplitude peak variation over a given ToF range (Figure 4a) could occur due to a physical shift in the location of a flaw, discontinuity or interface towards or away from the transducer due to material expansion or contraction. This would result in a delayed signal or prolonged ToF. Second, a change in the peak amplitude at a given ToF (Figure 4b) could be caused by a change in the physical properties of the materials at the interface leading to an increase or decrease in acoustic impedance mismatch at the interface. Finally, the complete loss of a peak (Figure 4c) indicative of the presence of a non-acoustically conductive layer, probably due to a severe defect, void, or loss of material component [78].

314



315
316 **Figure 4 Typical amplitude variations in ultrasonic analysis including (a) amplitude shift due to shift in interface along the**
317 **material thickness, (b) a measured increase in signal amplitude due to a higher acoustic impedance mismatch at a given**
318 **interface and (c) the complete absence of the interface being measured due to the presence of a non-acoustically conductive**
319 **layer [78].**

320
321 The ToF represents the time taken by the ultrasonic signal to reach the receiver or return to the transducer
322 in the pulse-echo mode. The ToF thus represents the change of ultrasonic velocity and/or thickness [79].
323 The greater the ToF, the greater the distance between the emitter and receptor for a given material with a
324 fixed V_p . The ToF is described by Equation 7, where L is the path length travelled, E is the Young's elastic
325 modulus, and ρ is the material density. The square root of E/ρ is the speed of sound, V_p through a given
326 medium.

$$327 \quad ToF = \frac{L}{V_p} = \frac{L}{\sqrt{\frac{E}{\rho}}} \quad (7)$$

328 In the case of pulse-echo measurements, the distance, L , will be twice the distance of the depth of the
329 material, d_i , at which the reflection signal was generated.

$$330 \quad ToF = \frac{L}{V_p} = \frac{2d_i}{V_p} \quad (8)$$

331 From the ToF, the time-of-flight shift (ToF shift) can be derived. This shift occurs due to changes in the
332 physical parameters of sample and can be observed when the acoustic signal is compared to a reference
333 signal [Figure 4(a)]. The relative intensities of the waveform can then be collated onto a heatmap or other
334 three-dimensional plots to show the waveform shift over time. The ToF shift is usually obtained using a
335 cross-correlation algorithm that matches the relative position of the initial waveform with each subsequent
336 ToF to show how much the waveform has shifted. Therefore, a more drastic shift due to a significant
337 physical change in a material will result in a greater ToF shift [80].

338 3.0 Application of Acoustic Methods for Diagnostics of Electrochemical Devices

339 3.1 Acoustic Diagnostics of Batteries

340 A growing number of studies have applied the AE technique for diagnostics in battery applications. In
341 batteries, the ion flow, electrode reactions and complex microstructures of the electrodes present many
342 sources of acoustic emission. In LIBs, for instance, the cathode consist of polycrystalline particles of active
343 materials, typically LiCoO_2 , LiFePO_4 or $\text{LiNi}_x\text{Mn}_y\text{Co}_z\text{O}_2$, mixed with a binder and conductive carbon,
344 which are made into a porous composite [81]. LIB anodes are typically formed from graphite, although
345 more exotic materials have been reported to show benefits in a range of areas [5,82,83]. During LIB
346 operation, Li^+ ions migrate to and intercalate into and out of the crystallites making up the active particles,
347 causing the materials to expand or contract. This volume change leads to stresses, cracks, and various stress-
348 induced degradation that can be exhibited at different length scales [84–87]. Figure 5 shows the various
349 degradation mechanisms that are often observed in operational LIBs.

350
351 The failure and degradation pathways of LIBs are generally assigned to three causes: inherent factors,
352 operational degradation and external causes. The inherent factors, which include SEI formation,
353 decomposition of the binder and degradation of the metal oxide components of the cell occur in all cells
354 with the extent of the degradation related (amongst other factors) to the age of the cells. External factors,
355 including the physical penetration of batteries or the exposure of cells to excessively high or low
356 temperatures can result in severe degradation or even cell failure [78–83]. Finally, the operational causes
357 of degradation may arise due to the design of battery systems. High power, or compact high-energy cells,
358 can be subjected to conditions that result in swelling and cracking of the electrodes. Over time this can
359 further manifest to a loss of Li inventory and electrode delamination [76,77,84]. Furthermore, the flux of
360 Li-ions is a nonequilibrium process that can cause concentration gradients in the material leading to the
361 development of stress and strain both inside the active material particles and in the surrounding composite
362 matrix [88]. The AE technique thus provides a non-destructive tool for the detection of degradation
363 originating from these mechanical and chemical processes. Gas evolution and the formation of cracks across
364 multiple length scales can be investigated with the extent and form of mechanical damage quantified,
365 allowing for the process and health monitoring in batteries.

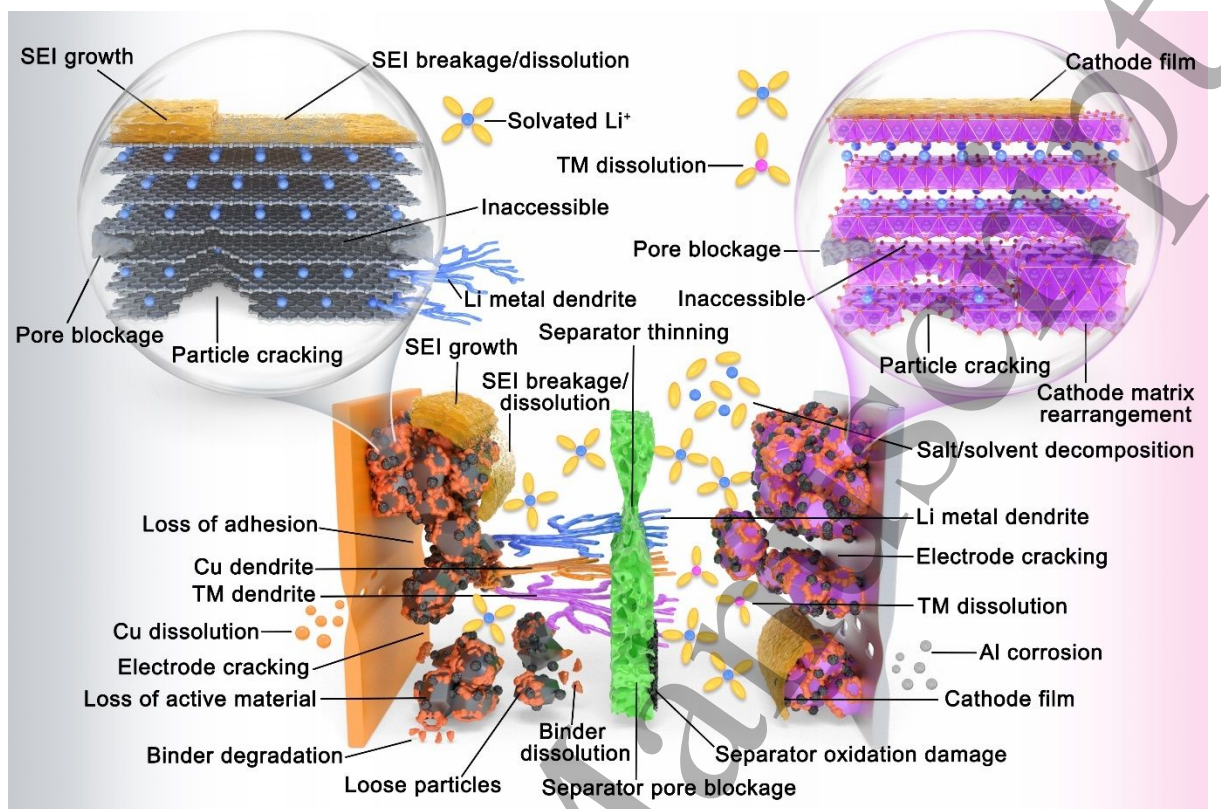


Figure 5 An outline of the most common degradation mechanisms in Li-ion batteries highlighting the highly complex and interconnected nature of the degradation phenomena in a cell.

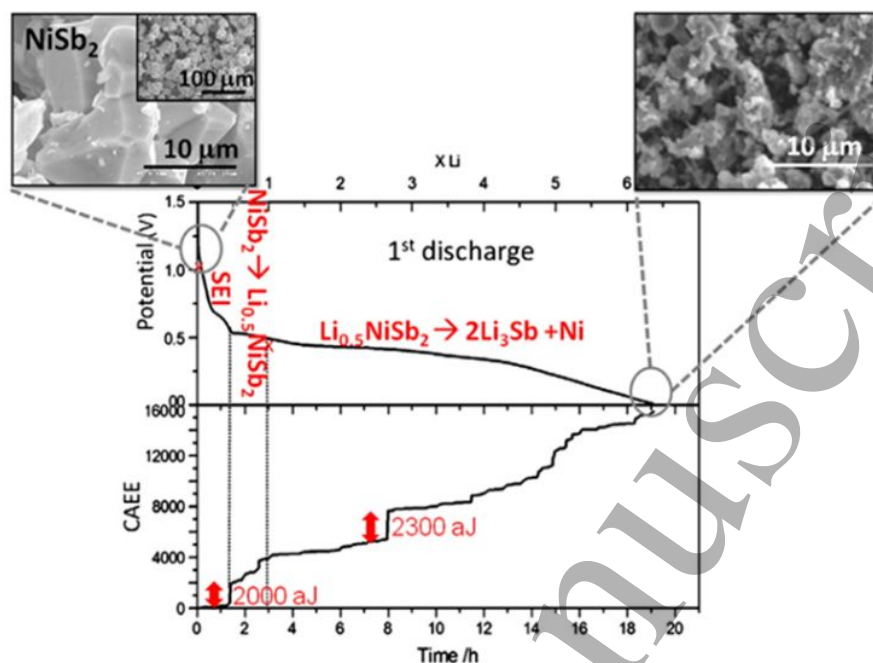
Based on the favourable mechanisms, the AE technique has been used in battery applications to identify mechanical damage *in operando* and evaluate the degradation of electrodes. Such work has been carried out on a range of battery chemistries, including metal hydride electrodes in Ni-MH batteries [89–91], MnO₂-based electrodes [92,93], Si-based electrodes [88,94], NiSb₂ electrodes [95] and the ubiquitous graphite-based electrode [96] in LIBs. In these studies, the cracking of the active material in the electrode and gas evolution have been identified as primary sources of AE signals. Each AE event is characterised using various parameters such as frequency, duration, cumulative energy etc. Therefore, various events (phenomena) can be isolated and classified according to their characteristic peak frequency obtained from the acoustic signal analysis. Gas evolution, which primarily occurs as a result of electrolyte degradation, has been observed typically between 80 kHz–250 kHz, with mechanical cracking reported at higher frequencies typically ranging from 250 kHz–400 kHz [89,97].

The earliest study, conducted by Ohzuku *et al.* [92], used the AE technique to investigate fracture in manganese dioxide cathodes used in Li/MnO₂ batteries during charge and discharge cycles. The results showed an increased number of acoustic events at higher discharge currents. In contrast, no events were

1
2
3 385 observed during charge, indicating that particle fracture occurs during Li-ion insertion into the solid
4 386 electrode matrix, with the rate of fracture proportional to the discharge current. In a subsequent study,
5 387 Ohzuku *et al.* [98] combined AE with a dilatometry technique (which measures thickness variation) to study
6 388 the correlation between acoustic events and the expansion of graphite electrodes in the first Li charge cycle,
7 389 using two electrolyte formulations. They identified a correlation between the expansion observed in the
8 390 solid graphite pellet and the acoustic events detected during the formation step, before the onset of
9 391 irreversible capacity loss. Analysis of the power spectrum of the acoustic events indicated that the signal
10 392 resulted from gas bubble formation. No significant acoustic events were identified during Li intercalation,
11 393 suggesting the initial events may be correlated to an initial solid electrolyte interface (SEI) formation.
12 394 Kircheva *et al.* [96] used the AE technique to study SEI formation and the first Li-ion intercalation on the
13 395 surface and inside the graphite electrode. The authors reported a significant increase in the cumulative
14 396 energy (CE) of the acoustic signal during SEI formation, alongside a positive correlation of the CE change
15 397 with SEI film resistance.

16 398
17 399 The AE technique has also been employed to investigate degradation in high-capacity LIB electrodes.
18 400 Matsuo *et al.* [97] studied LIB degradation using a clustering method based on applying waveform polarity,
19 401 power spectrum and enveloped waveform to identify various degradation mechanisms. The AE signals due
20 402 to gas evolution in the battery were detected continuously over the charging and discharging caused by
21 403 electrolyte decomposition on the graphite electrode surface during charge and discharge. In contrast, AE
22 404 signals due to damage to the graphite were observed near the potential plateau, caused by surface film
23 405 formation and phase transformation of graphite. Further, Villevieille *et al.* [95] used the AE technique to
24 406 monitor particle fracture in a conversion-type, NiSb₂ electrode material. The NiSb₂ electrode was cycled in
25 407 a Swagelok cell with a lithium foil used as a counter electrode, and the AE events monitored over three
26 408 cycles. The cumulative acoustic energy (denoted CAEE) obtained was then correlated with the
27 409 electrochemical activity. The result showed sudden jumps in CAEE at voltage plateaus corresponding to
28 410 SEI formation and active material conversion [Figure 6]. Cracking of the NiSb₂ particles was confirmed
29 411 using scanning electron microscopy which compared electrodes before cycling and after the first discharge.

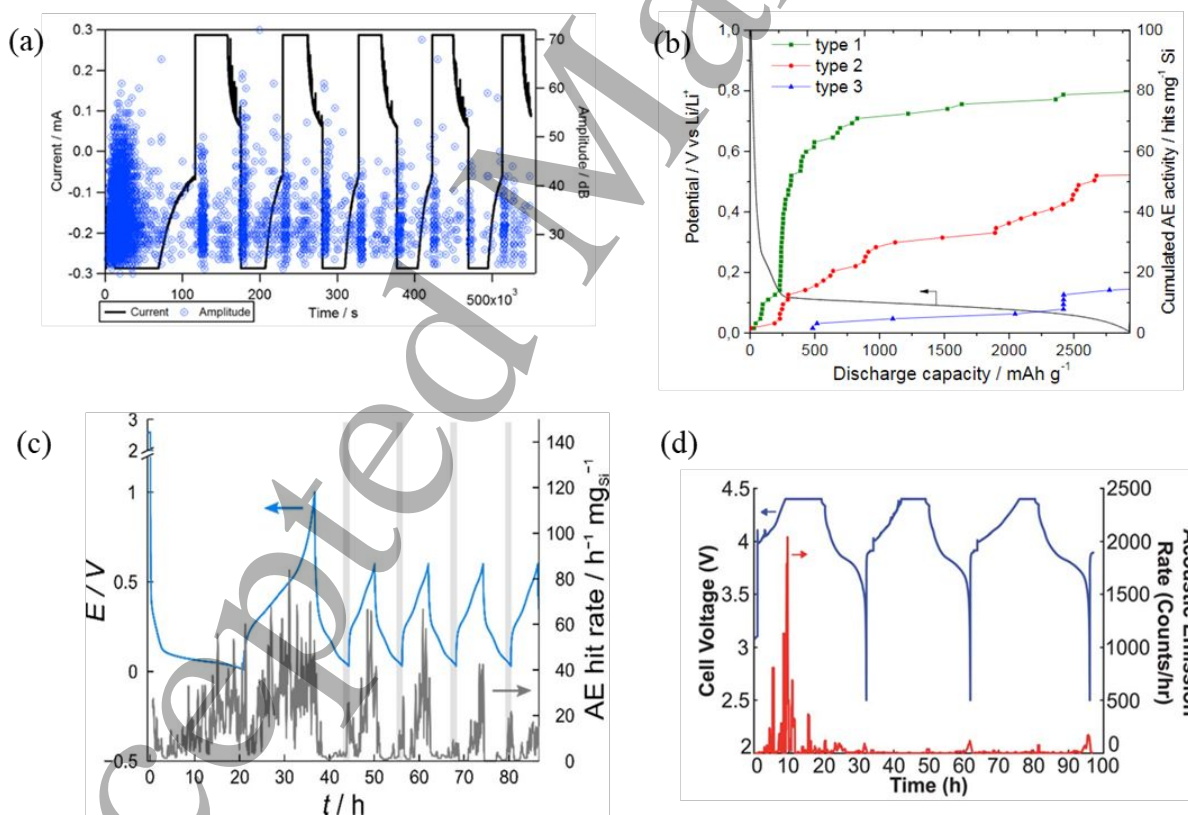
30 412
31
32
33
34
35
36
37
38
39
40
41
42
43
44
45
46
47
48
49
50
51
52
53
54
55
56
57
58
59
60



413
 414 **Figure 6. CAEE and voltage profile of the first discharge of NiSb_2/Li cell vs time (h), cycled at a C/10 rate between 1.5 and**
 415 **0.0 V. Left inset: SEM image of the starting NiSb_2 powder. Right inset: NiSb_2 -based electrode after a full discharge [95].**

416
 417 Silicon-based anodes, which offer the promise of increased capacity in LIBs, have also been investigated
 418 using AE techniques. When silicon is lithiated at room temperature, it can undergo a volume expansion in
 419 excess of 280%, which leads to extensive fracturing [99]. This is thought to be a primary cause of the
 420 accelerated capacity fade routinely observed [83]. A comprehensive understanding of material degradation
 421 in the anodes is necessary to identify processing and cycling techniques capable of reducing capacity fading
 422 and improve overall performance. Kalnaus *et al.* [100] examined the fracture of Si-particle during cycling
 423 of Li-ion half-cells with silicon electrodes. The authors built a thermal analogy model, using a brittle
 424 fracture damage parameter to predict stress and damage accumulation numerically. By combining the
 425 computational and experimental results at various particle sizes, the results suggested a micrometre-scale
 426 “critical fracture size” below which lithiation-induced fracture is not expected to occur. The work showed
 427 that the highest number of acoustic events was observed during the first discharge [Figure 7(a)] followed
 428 by distinct hits on subsequent charge and discharge cycles, suggesting that most of the particle
 429 fracture occurs during the initial insertion of Li ions. Rhodes *et al.* [88] monitored the acoustic response of
 430 composite silicon electrodes cycled in Li-ion half-cells. They showed that the major source of AE events is
 431 the surface fracture of the Si particles, resulting from the alloying reaction with Li that gives rise to Li_xSi
 432 phases which mainly occurs during the first lithiation. Distinct emission bursts were also observed on the
 433 subsequent charge and discharge step. Tranchot *et al.* [94] also investigated the mechanical degradation of

434 Si-based electrodes for Li-ion cells using the AE technique. Three distinct populations of acoustic signals
 435 (labelled Type 1, 2 and 3 in Figure 7b) were identified and found to result from electrode cracking
 436 accentuated by the formation of the $c\text{-Li}_{15}\text{Si}_{14}$ phase. Once again, the AE signal was primarily detected
 437 during the first lithiation as the electrode cracking mainly occurs during the first discharge. However, the
 438 AE activity increased at the end of the discharge when the $c\text{-Li}_{15}\text{Si}_4$ phase is formed and during the charge
 439 when the potential reaches ~ 0.45 V, corresponding to the delithiation of $c\text{-Li}_{15}\text{Si}_4$. Recently, Schiele *et al.*
 440 [101] studied the gassing behaviour, volume expansion, and mechanical degradation of Si/C composite
 441 electrodes using the AE technique combined with mass spectrometry. They reported a strong variation of
 442 the rate of acoustic events with cell potential with most of the acoustic hits detected in the first cycle (Figure
 443 7c). Also, interestingly, they reported a higher acoustic activity during delithiation than during lithiation in
 444 contrast to studies by Rhodes *et al.* [88] and Tranchot *et al.* [94] where the majority of the acoustic events
 445 were observed upon lithiation. Overall, the AE activity decreased with cycling, indicating that most of the
 446 mechanical degradation occurs in the first couple of cycles.

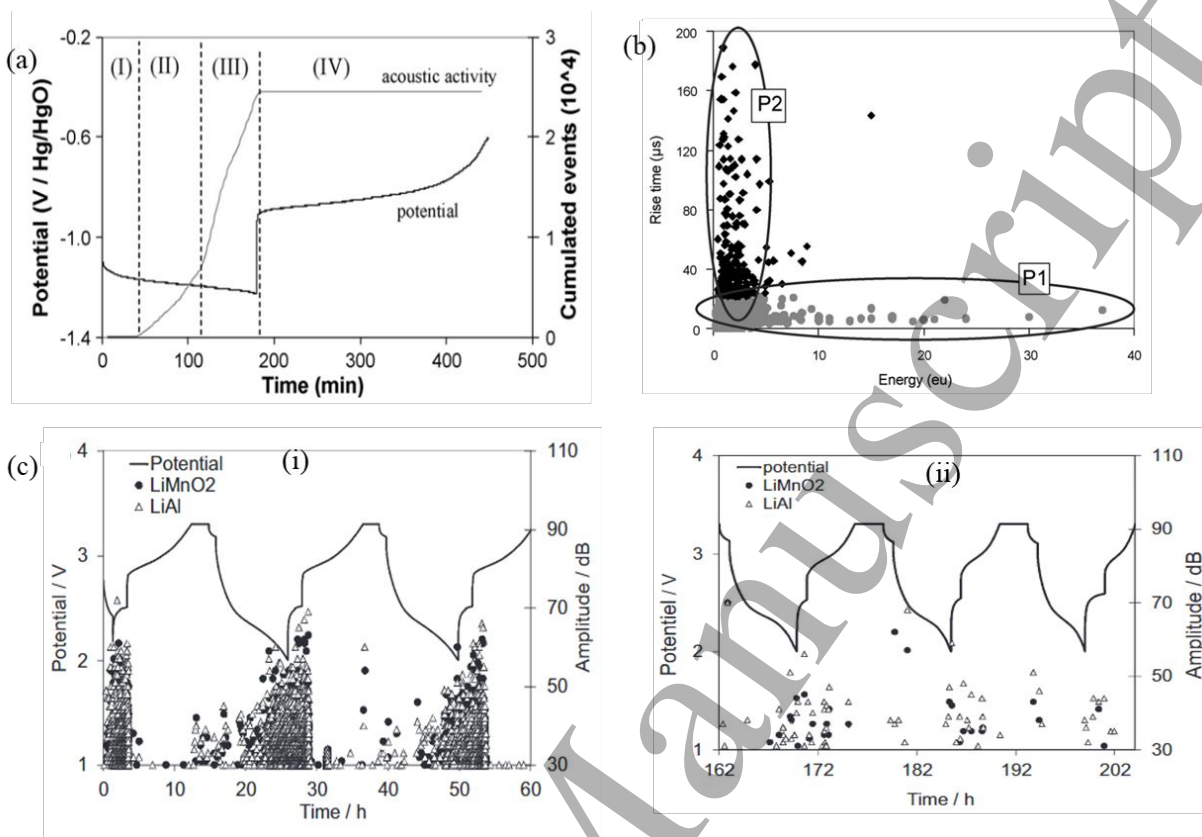


448
 449 **Figure 7** (a) AE data for electrochemical cycling of Si anode showing evolution of acoustic signal (blue) over charge cycles
 450 [100]. (b) Evolution of the electrode potential and acoustic activity of type 1, 2 and 3 signals during the first discharge in Si
 451 anodes [94]. (c) Cell potential (blue) and AE hit rate (grey) during AE measurement on the Si/C composite-containing
 452 electrode. The cell was assembled with the Li metal and LP57 as the counter electrode and electrolyte, respectively. The
 453 region close to the lower cutoff potential is highlighted for clarity [101]. (d) Cell voltage (blue) and acoustic emission rate

1
2
3 454 (red) measured during the first three cycles of a LiCoO₂ sintered electrode. Acoustic emission events are highly concentrated
4 455 in the first charge cycle [102].
5
6 456

7 457 Similar results have been reported in other electrodes. Woodford *et al.* [103] studied damage evolution in
8 458 LiCoO₂ cathode using micromechanical models corroborated by *in situ* AE experiments. They attributed
9 459 the fracture and mechanical degradation of polycrystalline Li-storage materials to shape changes upon
10 460 lithium (de)intercalation of the polycrystalline microstructure. Furthermore, the most pronounced AE bursts
11 461 were observed in the middle of the first charge cycle with a smaller burst observed at the end of each
12 462 discharge cycle [Figure 7(d)]. Inoue *et al.* [91] used the AE technique to monitor the processes occurring
13 463 at MmNi_{3.6}Mn_{0.4}Al_{0.3}Co_{0.7} (Mm = mischmetal) alloy negative electrodes *in situ*. They reported two distinct
14 464 classes of AE waveform: the first, which has a long duration, relatively narrow frequency distribution and
15 465 lower maximum amplitude was attributed to hydrogen evolution; and a second burst-type waveform having
16 466 shorter duration, wide frequency distribution and large amplitude was attributed to cracking of the alloy
17 467 particles.
18
19 468

20 469 Similarly, Didier-Laurent *et al.* [104] studied particle cracking during charge/discharge cycling of two metal
21 470 hydrides (MH) alloy electrodes using the AE technique. Correlation of the acoustic activity with the
22 471 electrode potential during charge/discharge showed four stages of acoustic activity [Figure 8(a)]. Stages I
23 472 & IV of low acoustic activity at the start of charging and during discharge, respectively; and Stage II and
24 473 III, where the acoustic activity increases progressively attributed to particle cracking and gas evolution,
25 474 respectively. In both alloys studied, two distinct populations of acoustic signals were detected during
26 475 charging steps [Figure 8(b)]. The first group (labelled P1) was characterised by high energy and short rise
27 476 time, and higher peak frequencies between 230 and 260 kHz. The second group (labelled P2) showed lower
28 477 energy, longer rise time and lower peak frequencies between 150 and 180 kHz. The first group of acoustic
29 478 events were attributed to the cracking of the MH particles. In contrast, the second group with low
30 479 characteristic energy was ascribed to the hydrogen evolution reaction. No acoustic activity was detected
31 480 during discharge. In a follow-up study using both alloys, Etienneble *et al.* [89] further investigated the
32 481 evolution of the AE signals related to both the metal-hydride particle cracking and those due to hydrogen
33 482 gas evolution as a function of the charge input in the two metal alloy electrodes. They reported more
34 483 significant cracking phenomena in the LaNi₅-based electrode (~5–25 mAh g⁻¹) than for the MgNi electrode
35 484 (~365 mAh g⁻¹) at lower charge input, indicating different cracking mechanisms in the alloys. In a further
36 485 study, Etienneble *et al.* [90] studied the pulverisation of LaNi₅-based electrodes with different Co contents
37 486 by *operando* AE measurements and demonstrated that cracking of the electrode occurs mostly during the
38 487 first charge.
39
40
41
42
43
44
45
46
47
48
49
50
51
52
53
54
55
56
57
58
59
60



488
 489 **Figure 8.** (a) Typical evolution of the AE activity vs. time recorded during a charge/discharge cycle on a LaNi₅-based
 490 electrode [104]. (b) Rise time vs signals energy recorded during charging at 100 mA g⁻¹ on a LaNi₅-based electrode. (c)
 491 Voltage profile on cycling and AE activity in terms of counts (C) versus time recorded for (i) the first three cycles and for
 492 (ii) the last three cycles, from a total of 30 cycles [93].

493
 494 To gain a better understanding of mechanisms in the Li/S battery systems, Lemarié *et al.* [60] investigated
 495 the mechanical degradation of sulphur-based electrodes during cycling using the AE technique. Comparing
 496 the AE response under various combinations of binders and current collectors showed prominence of the
 497 AE signals under three specific cases. Firstly, during first discharge, attributed to the initial dissolution of
 498 elemental sulphur into the electrolyte; secondly, at the end of charge where sulphur formed on the electrode
 499 surface and a third cluster at the end of discharge when the cell was seen to polarise excessively attributed
 500 to an inefficient reformation of the sulphur electrode. Barai and Mukherjee [105] developed a computational
 501 methodology to study the acoustic response of microcrack formation in LiB electrodes. They reported the
 502 energy released due to electrode fracture as the primary source of acoustic emission response. Kircheva *et*
 503 *al.* [93] used the AE technique for the ageing characterisation of a LiAl/LiMnO₂ cell. They reported a
 504 decrease of acoustic activity with cell ageing [Figures 8(c) and (d)], attributed to the degradation of active
 505 materials which do not entirely participate in the electrochemical reactions. Also, the AE events were found

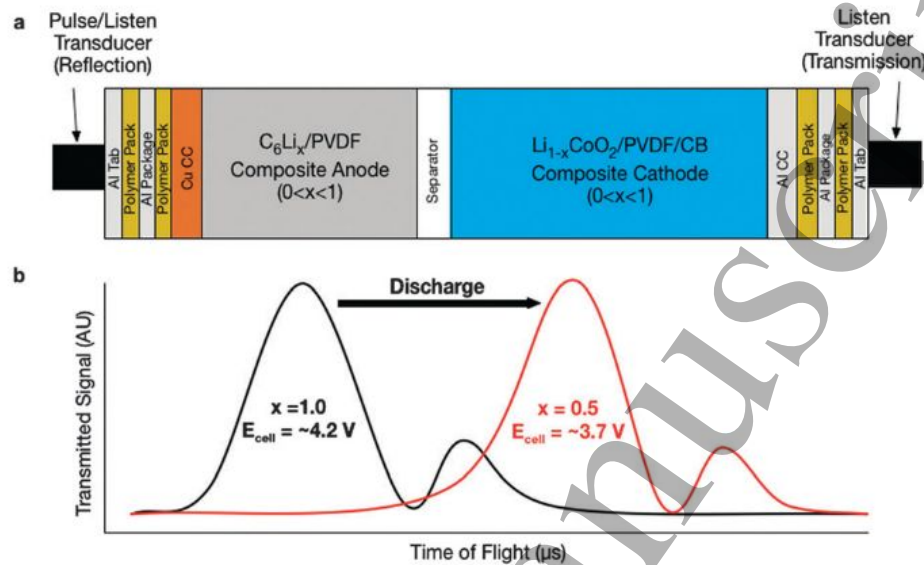
506 to be more pronounced during discharge attributed to phase transformation as well as intercalation of
507 lithium ions.

508
509 Degradation in commercial cell formats has also been monitored using the AE technique [106]. A
510 commercial 18650 battery and a model half cell (Li/organic electrolyte/LiCoO₂) were compared during
511 charge and discharge cycling. In the commercial battery, AE events were detected during every discharging
512 process at SoC of around 35% and 15%, attributed to the fracture of LiCoO₂ particle by phase transition. In
513 the model half cell, AE events were found during initial cycles in the charging process due to the SEI
514 formation; however, in the discharge process, this was only detected under high C-rates. Recently, Tang *et*
515 *al.* [107] studied the three-point bending failure process in a commercial 18650 lithium-ion cell using the
516 AE technique. The resulting acoustic analysis showed three main types of damage produced by the three-
517 point bending process, namely: electrode delamination, interlayer slip, and electrode and separator
518 cracking.

519
520 Whereas AE techniques can passively identify defects, particle cracking and gas evolution in cells, dynamic
521 ultrasonic testing offers significant promise for process and health status monitoring in battery systems. The
522 UT technique allows practical determination of processes and the internal state of batteries based on the
523 fact that batteries are primarily composite material systems which undergo chemical and mechanical
524 evolution, including variations in lithiation state, delamination, cracking, etc., during cycling and ageing.
525 These chemical and structural changes lead to changes in material properties (mass densities and moduli)
526 which in turn influences the ultrasonic impedances and ultrasonic velocity, allowing prediction of important
527 cell parameters such as the SoC and SoH [80,108]. The concept of the ultrasonic testing approach in battery
528 diagnostic is illustrated for an example cell in Figure 9.

529
530 Studies have shown that changes in the acoustic ToF of the ultrasound signal are linked to physical changes
531 in the electrodes (density and modulus), which could be used to measure the SoC of batteries [109]. In
532 Zn/MnO₂ cells, changes in the acoustic waveforms from ultrasonic measurement have been shown to
533 correlate with dehydration of the Zn gel anode, the formation of ZnO and physical transitions that occurs
534 during discharge [110]. In vanadium redox flow battery (VRFB), the ultrasonic velocity has been shown to
535 correlate with changes of vanadium ion compositions in the positive electrolyte solution as the SoC of the
536 VRFB varied, allowing for SoC prediction [111]. In LIBs, changes in acoustic ToF have been used to study
537 SEI formation and capacity degradation [80], internal structure changes during charging [112,113], anode
538 and cathode structure during charge and discharge at high rates [76], and identification of macroscale
539 defects in electrode layers [78,114]. These studies highlight the potential deployment of acoustic imaging

540 into in-line quality control monitoring systems for batteries, with the tool also having the promise of
 541 screening batteries before second-life deployment to ensure the safety of cells.



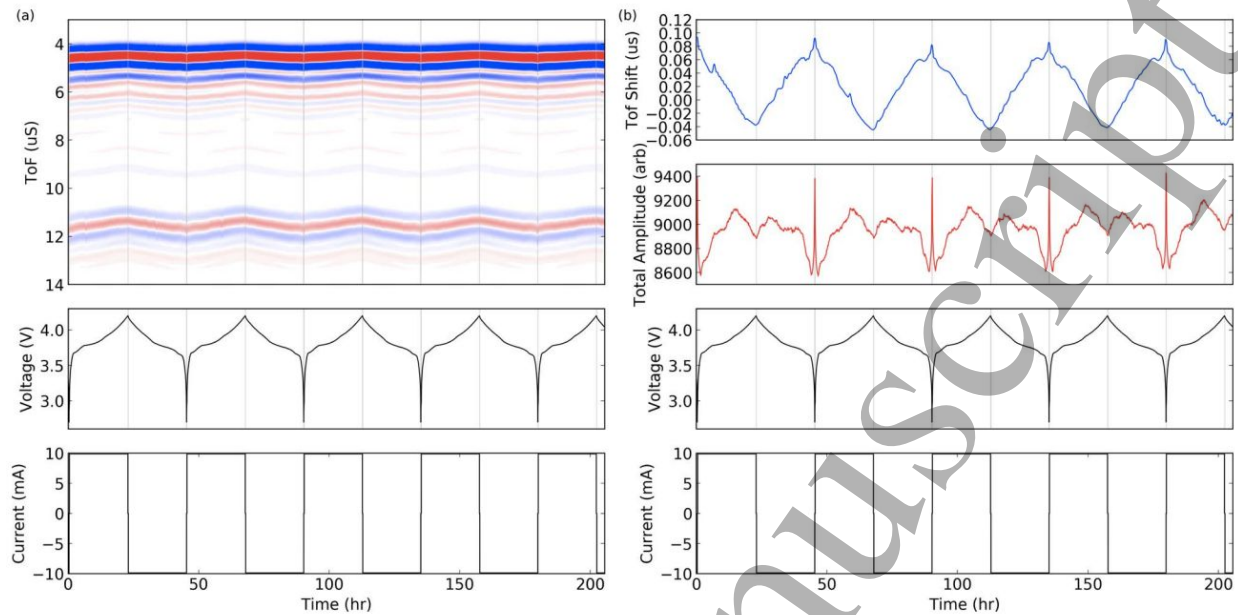
542
 543 **Figure 9. Ultrasonic interrogation of a representative battery. (a) Schematic representation of a battery with the various**
 544 **packaging, current collector, electrode, and separator layers as well as the two acoustic transducers (pulse/listen and listen)**
 545 **for ultrasonic interrogation. (b) Example illustration of the increase in ToF of the transmitted signal as a function of SoC**
 546 **that occurs during discharge; this shift results from the changes in electrode densities as the SoC (i.e., Li content, x) changes**
 547 **[109].**

548
 549 During battery cycling, electrochemical changes within the host intercalation materials result in mechanical
 550 properties changes, which leads to shifts in the ToF of the ultrasonic signal. Several studies have shown
 551 that the SoC increase as lithiation proceeds during cell charging is detected as a decrease in the acoustic
 552 ToF [75,76,79,109,112,115–118]. Hsieh *et al.* [109] performed ultrasonic ToF analysis of commercial
 553 $LiCoO_2$ /graphite pouch cell and suggested that during cell charging, the acoustic intensities (signal
 554 amplitude) decrease slightly initially as the hexagonal-to-monoclinic phase transformation of the $LiCoO_2$
 555 is reversed, then increase steadily with an increase in the SoC. In the study, the ToF peaks were observed
 556 to shift towards lower values and higher intensities during charge. A consistent feature at $>4V$ cell potential
 557 at the end of charge, was a slight increase in acoustic absorption, attributed to two-phase staging reaction
 558 of the $LiCoO_2$ cathode which alters its density significantly. This finding was echoed by Davies *et al.* [75],
 559 who showed that as the cell charges, the acoustic waveform shifts to a lower ToF seen as the wave moving
 560 upward during charge in the top image of Figure 10(a). Ladpli *et al.* [115] attributed the decrease in ToF
 561 during cell charging to faster wave speed with increasing SoC which leads to increased modulus and/or
 562 declining stiffness, in agreement with results from literature which shows that the density of graphite anode
 563 [119] and cathode [120] decreases and the modulus increases [85] during charging. The authors further

1
2
3 564 demonstrated that the signal amplitude intensifies with increasing SoC except at the beginning and end of
4 565 charging. Other studies by Glanz *et al.* [118], Robinson *et al.* [76,112], and Wu *et al.* [79] have
5 566 demonstrated a general decrease in the acoustic ToF during cell charge.
6
7

8 567
9 568 During cell discharging, Hsieh *et al.* [109] showed that acoustic absorption increases (i.e., the transmitted
10 569 and reflected intensities decrease) except at the end of discharge at a cell potential <3.5 V, where the signal
11 570 intensities increased dramatically, attributed to the hexagonal-to-monoclinic phase transformation of the
12 571 LiCoO_2 which alters the modulus and density of the cathode. Also, the ToF peaks shift towards higher
13 572 values and lower intensities during discharge. Davies *et al.* [75] also showed a shift to higher ToF as cell
14 573 discharges [Figure 10(a)]. The result showed a notable drop off in amplitude below $\sim 25\%$ of SoC, followed
15 574 by a spike in amplitude at the bottom of charge. The significant and rapid change in the ToF shift and signal
16 575 amplitude at the bottom of charge was suggested to indicate structural changes at this level of discharge
17 576 and sign of over-discharge of the cell. Similarly, Ladpli *et al.* [115] showed that the ToF increases and the
18 577 signal amplitude decrease during discharging. Studies by Robinson *et al.* [76] and Wu *et al.* [79] have
19 578 further confirmed that the acoustic ToF increased and the signal amplitude decreased uniformly during cell
20 579 discharge until the end of discharge. Generally, as the battery discharges, lithium de-intercalates from the
21 580 anode and intercalates into the cathode, which decreases the elastic moduli for the electrodes, which
22 581 according to Equation 7, will reduce the ultrasonic velocity and cause the increase of ToF during the
23 582 discharging process.
24
25
26
27
28
29

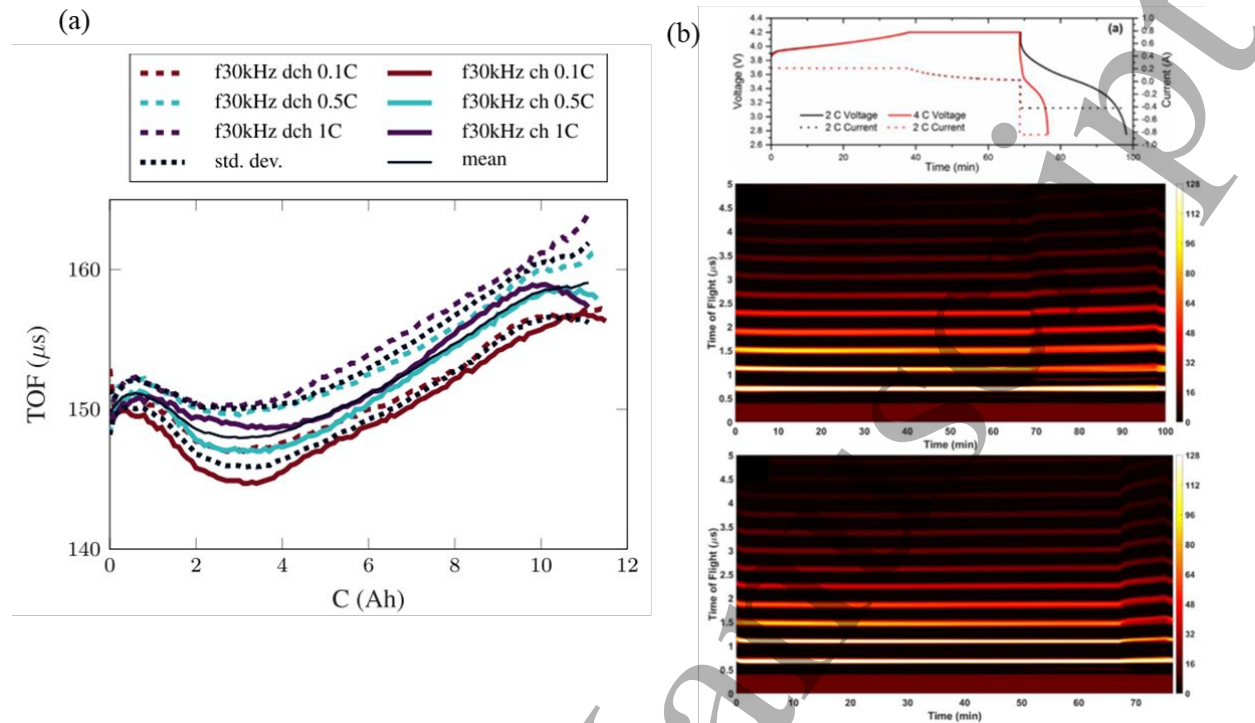
30 583
31 584 In general, cycling behaviour as studied by Hsieh *et al.* [109], Davies *et al.* [75], Ladpli *et al.* [116],
32 585 Robinson *et al.* [76] and Knehr *et al.* [121] show clear and repeatable trends in the ultrasonic waveforms,
33 586 which vary periodically, synchronised with the electrochemical cycling (Figure 10). Abrupt changes in
34 587 signal amplitude or ToF often near the end of charge or discharge has been attributed to the scarcity and
35 588 excess of lithium ions respectively, causing abrupt stiffness changes [109]. Also, the general trend was a
36 589 decrease in ToF of the ultrasonic signal with increasing cycles as well as fading of the signal amplitude
37 590 across cycles. This is important as it allows SoC prediction based solely on ultrasonic analysis and
38 591 highlights the potential of the technique to provide information about the SoH of the cell over an extended
39 592 period. Model prediction of SoC and SoH in these studies have reported SoC prediction to within $\sim 3.5\%$
40 593 [113], and $\sim 1\%$ accuracy [75] for both lithium cobalt oxide and lithium iron phosphate cells, and SoH to
41 594 within an error of $\sim 1\%$ [75].
42
43
44
45
46
47
48
49
50
51
52
53
54
55
56
57
58
59
60



595
 596 **Figure 10. (a) Representative ultrasonic signal during cycling for several cycles of a lithium-cobalt oxide pouch cell at a**
 597 **C/20 charge/discharge rate. The ToF heat map shows maximum and minimum waveform amplitudes in red and blue,**
 598 **respectively. (b) The same ultrasonic data reduced to a ToF and amplitude metric. The blue and red lines represent the**
 599 **single ToF shift and amplitude measures, respectively [75].**

600 Cycle rates, commonly expressed as a C-rate, indicates the theoretical number of hours needed to charge
 601 or discharge a cell completely. For example, a rate of 1C corresponds to a complete charge or discharge in
 602 1 h, and a rate of C/20 would indicate a theoretically complete charge or discharge in 20 h. Studies have
 603 shown that ToF responses differ at different C-rates as changes in C-rates could lead to changes in the
 604 mechanical behaviour of the cell as the electrochemically-induced stresses and strains in the battery
 605 electrodes are expected to become more significant during high-rate charging and discharging [76]. Popp
 606 *et al.* [118] reported longer ToFs at higher C-rates and a pronounced local minima in the ToF at low C-rates
 607 (Fig 11a) attributed to inhomogeneous lithium distribution within the electrodes. A similar result by
 608 Robinson *et al.* [76] showed an increase in the slope of the ToF shift at higher C-rates (Figure 11b),
 609 attributed to the higher electrochemical stiffness (a measure of the electrochemically induced change in
 610 Young's modulus) observed under these conditions, also as reported by Tavassol *et al.* [122]. The authors
 611 also observed an initial decrease in the ToF peak locations at all C-rates, followed by an increase in the ToF
 612 during the discharging phase.

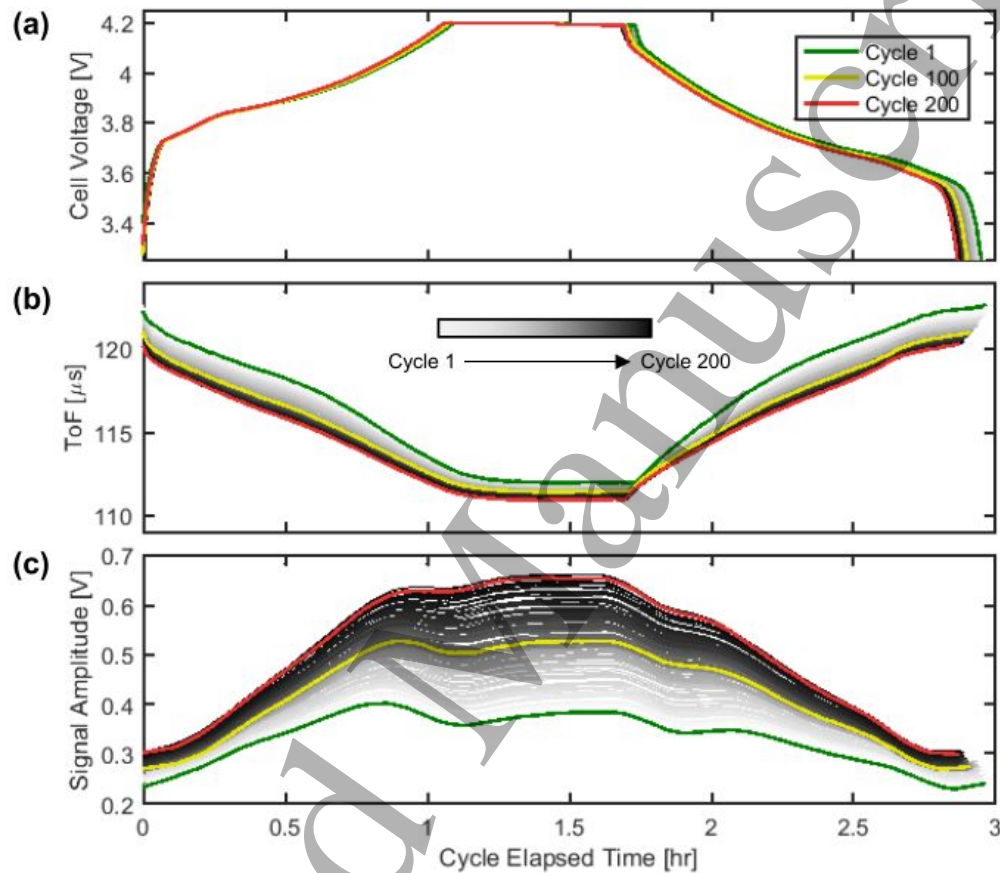
613



614
615
616 **Figure 11. (a) ToF for charge (ch) and discharge (dch) at different C-rates [118]. (b) Top: Electrochemical response for 1C**
617 **charge, 2C discharge and 1C charge, 4C discharge cycles. Middle: Acoustic signal response for (b) 1C charge, 2C discharge**
618 **and Bottom: 1C charge, 4C discharge cycles. The acoustic ToF spectra show the acoustic amplitude (measured in AU) and**
619 **acoustic ToF response of the acoustic measurements during the full discharge cycles and periods during which the cell is**
620 **allowed to maintain an open circuit potential [76].**

621
622 Ultrasonic characteristics during prolonged cell cycling have been investigated using the two main
623 ultrasonic parameters, namely signal amplitude and ToF [79,109,116,123]. Ladpli *et al.* [115] demonstrated
624 that ToF shift towards a lower value, i.e. slower wave speed, with increasing cycle number, with the shift
625 more notable towards the end of discharge and at the beginning of charge [Figure 12(b)]. The decline in
626 ToF was seen to be more dramatic during the first 100 cycles than during the later 100 cycles. On the other
627 hand, the signal amplitude gradually intensifies at all SoC as the cycle count increases [Figure 12(c)]. The
628 amplification in the signal amplitude was shown to be less dramatic at the end of discharge and beginning
629 of charge than elsewhere. The change in ToF and signal amplitude was ascribed to moduli and densities
630 changes due to battery degradation. Lower ToF and higher signal amplitude suggests that aging might
631 increase the battery's overall stiffness and/or lower density. On the other hand, Sood *et al.* [123] reported
632 that the amplitude of the input ultrasonic pulse is weakened as the cell is cycled, attributed to the degradation
633 of interfaces inside the cell caused by electrode expansion, gas evolution, or stress developing along the
634 interfaces. Similarly, Wu *et al.* [79] showed that the ToF increases as the battery degrade and that the signal

635 amplitude generally increases then decreases after long cycling attributed to possible gas generation inside
 636 the battery [21]. Gas exhibits significantly higher attenuation than liquids or solids as it is inferior at
 637 transmitting ultrasonic signals. Thus gas generation is seen as a reduction in acoustic intensity or loss of
 638 reflected signal during ToF analysis.

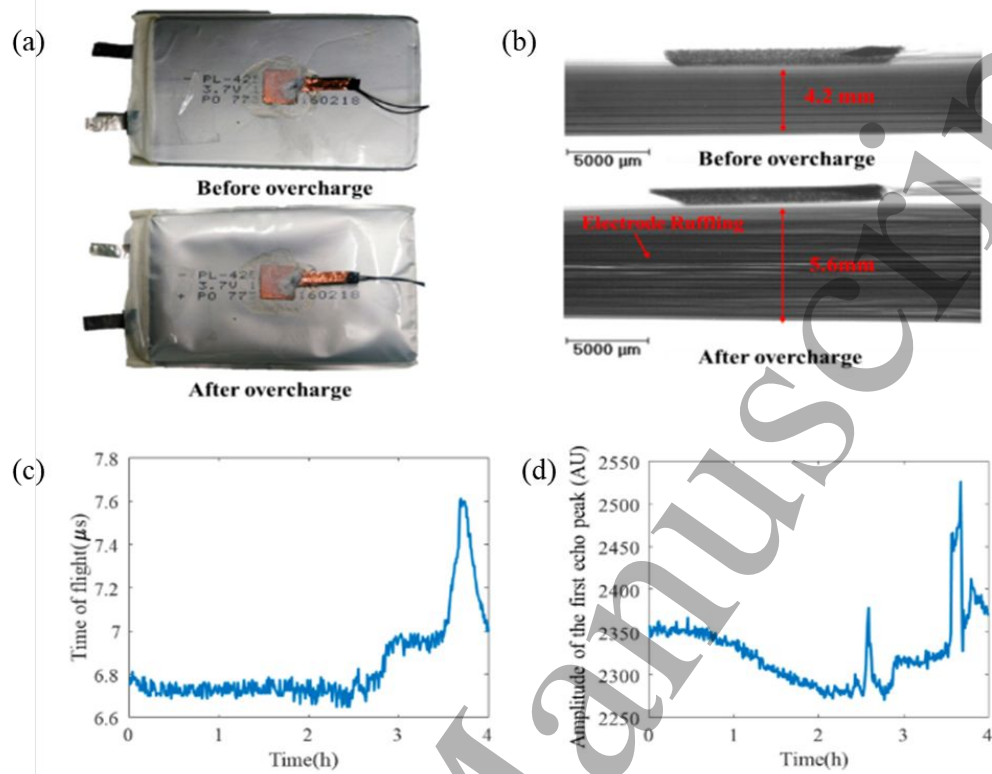


639
 640 **Figure 12. Cycle-to-cycle evolution of (a) cell voltage (b) ToF, and (c) signal amplitude, due to electrochemical ageing shown**
 641 **in progressive shades of grey as a function of cycle elapsed time. Data from the first cycle is indicated in green, the 100th**
 642 **cycle indicated in yellow, and the 200th cycle indicated in red [115].**

643
 644 For greater reliability and, hence, increased battery technology adoption, the development of diagnostics
 645 for better monitoring of battery health and early prediction of failure is a key requirement. Various studies
 646 have used the UT technique for the investigation of acoustic behaviour during cell failure. Davies *et al.* [75]
 647 demonstrated significant shifts in the ultrasonic signals during cell failure, as well as a decrease in the signal
 648 amplitude. The ultrasonic signal amplitude faded significantly following failure once the cell passes the
 649 bottom of charge attributed to electrolyte breakdown and cell gassing. Wu *et al.* [79] performed an
 650 overcharge-induced battery failure where voltage (up to 5 V) was forced onto a 1.8 Ah battery after
 651 prolonged cycling to investigate the ultrasonic signal behaviour under severe abusive condition. Figure

1
2
3 652 13(a) shows the top view of the battery before and after overcharge. Figure 13(b) shows the X-ray images
4 653 (the side view) of the battery. The ultrasonic features during the overcharge test are shown in Figure 13(c)
5 654 and (d). As seen in Figure 13(c), the ToF shifts towards the lower value before 2.5 h, in agreement with
6 655 behaviour often observed during charging. The ToF then begins to increase sharply after 2.8 h and about
7 656 4.7V, attributed to gas generation inside the battery as well as the increase in the thickness of battery layers.
8 657 A sharp rise in peak amplitude was also observed as the cell overcharged [Figure 13(d)]. Pham *et al.* [124]
9 658 also investigated electrode delamination and gas formation in lithium-ion batteries during thermal abuse on
10 659 210 mAh commercial lithium-ion pouch cells using a range of techniques including ultrasonic ToF analysis,
11 660 fractional thermal runaway calorimetry and synchrotron X-ray imaging. During the gradual thermal abuse,
12 661 a trend of delayed ToF of the ultrasonic wave was observed during the onset of heating at ca. 6 min 20 s
13 662 into the test, as shown in Figure 14(a). This was attributed to decreased density with increasing temperature
14 663 and, therefore, lower ultrasonic wave propagation. A slower propagation of thermal runaway and a less
15 664 catastrophic failure was seen to lead to a more gradual ToF shift and a slower loss of acoustic signal, as
16 665 seen in Figure 14(b). However, slower thermal runaway propagation lead to prolonged gas generation and
17 666 therefore longer time (ca. 11 min to 16.5 min) during which the ultrasonic signal was lost. Zappen *et al.*
18 667 [125] used the ultrasonic technique to study high-temperature abuse on a nickel-manganese-cobalt oxide
19 668 (NMC)/graphite lithium-ion battery cell. The results showed the responsiveness of the ultrasonic
20 669 measurements to safety-critical degradation effects which happens during exposure to high temperatures.
21 670 As ultrasonic signals vary distinctively with varying temperature, this technique helps capture phenomena
22 671 occurring at different temperature ranges, such as SEI dissolution, evaporation of solvent, among others,
23 672 that have been well-documented in literature.

24
25
26
27
28
29
30
31
32
33
34
35 673
36
37
38
39
40
41
42
43
44
45
46
47
48
49
50
51
52
53
54
55
56
57
58
59
60

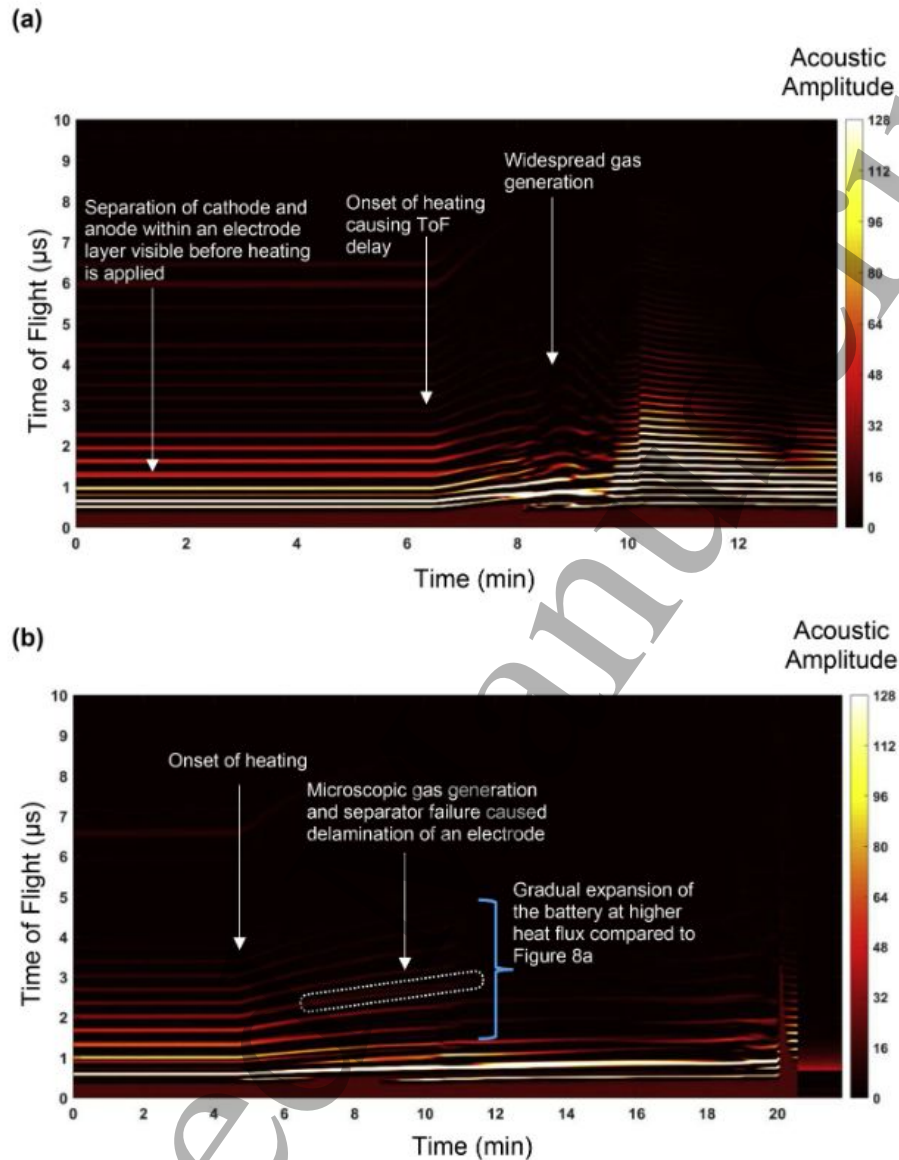


674

675 **Figure 13. Overcharge test results for battery: (a) photos of the battery (top view), (b) X-ray CT images of the battery (side**
 676 **view), (c) evolution of ToF, and (d) evolution of the first echo peak amplitude [79].**

677

Accepted Manuscript



678

679

680 Figure 14 (a) ToF spectrogram of 210 mAh commercial pouch cell during the first failure test, with highlighted regions of
 681 interest during induced thermal runaway. The onset of heating occurs at approximately 6 min 20 s into the test. (b) ToF
 682 spectrogram of 210 mAh commercial pouch cell with highlighted regions of interest during thermal runaway. The onset of
 683 thermal runaway at approximately 4 min 20 s into the test with the main features of interest identified. The acoustic
 684 amplitude is displayed in arbitrary units [124].

685

686 LIBs are expected to cycle in environments with wide temperature variations. This is an essential
 687 consideration in building battery management systems for mobile or outdoor stationary applications where
 688 temperature extremes are expected. From an acoustic viewpoint, warmer temperatures would lead to
 689 changes in Young's modulus of materials within the battery and, therefore, in the sound propagation speed.

690

691

692

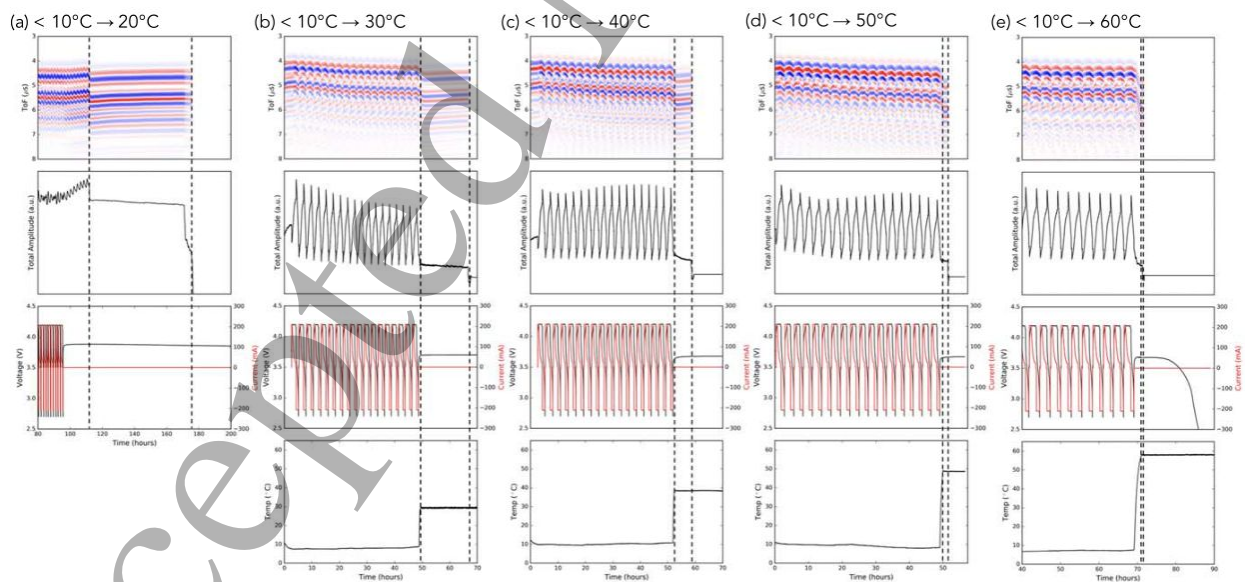
693

694

695

696

690 Studies have investigated acoustic behaviour as a result of temperature change within the cell. Robinson *et al.* [76] demonstrated that an increase in temperature from 25 to 30 °C showed only slight changes in the acoustic intensity attributed to slight variations in Young's modulus, with no significant change in the ToF, 691 692 693 unsurprising given the relatively little temperature change. More recently, Chang *et al.* [126] investigated LiCoO₂/graphite LIBs over a wider temperature range from a 0–60 °C environment during cycling (Figure 15) and demonstrated through UT analysis that LiCoO₂/graphite LIBs experience catastrophic failure when moved across this temperature range during cycling. This is based on the existing understanding that lithium plating of the graphite anode occurs below 10 °C at typical 1C charge rates and that LiPF₆ electrolyte decomposition begins to occur at 60 °C and higher [127]. In addition to noticeable physical bulging of the pouch cell, ultrasonic signals transmitted through the battery provide evidence of when gassing occurs, as the ultrasonic waves are dramatically attenuated in the presence of a gaseous medium due to a high acoustic impedance mismatch. In all cases, as seen in Figure 15, the initial temperature shift, shown by the first dotted line, results in a corresponding shift of the acoustic waveforms due to temperature effects on sound transmission. Subsequently, the acoustic signal loss was observed for all temperature shifts. Similarly, Bommier *et al.* [128] explored the use of the UT technique for gassing and lithium plating detection at lower temperatures. The results showed that period of visible gassing and swelling correlated well with permanent attenuation of the acoustic signal.



708
709 **Figure 15. Acoustic and electrochemical data of 210 mAh pouch cells initially cycled at cold (<10 °C) temperature to induce**
710 **plating, before the environmental temperature was shifted higher to (a) 20 °C, (b) 30 °C, (c) 40 °C, (d) 50 °C, and (e) 60 °C**
711 **while keeping the cell at open circuit potential and bottom-of-charge. For each condition, plots are shown for the heatmap**
712 **of the acoustic waveforms superimposed over time on the x-axis (the acoustic ToF), the total amplitude vs time, the**

1
2
3 713 voltage/current profiles, and the environmental temperature in the incubator as measured by a thermistor. The dotted lines
4 714 indicate the time range starting from the temperature shift until loss of signal was observed. [126].
5
6

7 715 3.2 Acoustic Diagnostics of Redox Flow Batteries

8
9 716 In redox flow batteries, external electrolyte tanks containing two soluble redox couple are pumped through
10 717 flow-through electrodes contained within a stack and separated by an ionic conducting membrane. In this
11 718 set-up, the SoC, determined by the concentration of the electro-active ion in each solution, is a critical
12 719 indicator of battery health. Thus, SoC estimation is of vital importance for long-term, safe operation. Direct
13 720 measurement of these concentrations online during cell operation is challenging. Currently, one of the most
14 721 common approaches for SoC estimation relies on the measurement of the open-circuit voltage (OCV).
15 722 Although this technique is fast and easy, it gives only an indication of the SoC of the system and no
16 723 information on the individual electrolyte solutions. However, degradation mechanisms in RFBs can often
17 724 be asymmetric, affecting one of the electrolyte solutions disproportionately, thus creating a capacity
18 725 imbalance between the catholyte and anolyte [111]. Therefore, accurate and reliable methods for monitoring
19 726 the individual SoC of each electrode is highly desirable.
20
21
22
23
24
25

26 727
27
28 728 As initial studies have shown, ultrasonic testing provides a promising solution for monitoring the individual
29 729 SoC of the positive and negative electrolyte solutions. The large changes in solution viscosity with the
30 730 electrochemical conversion of the species in each electrolyte solution mean that there are significant
31 731 changes in the speed at which sound will travel through the solution. The first such study by Chou *et al.*
32 732 [111] used the ultrasonic testing technique to monitor the SoC of vanadium RFBs. Using a through-
33 733 transmission set-up, the authors showed an increase in the SoC of the VRFB correlated to an increase in
34 734 the ToF of the ultrasonic signal. Although, due to the close relationship between the properties of a solution
35 735 and the temperature, temperature could significantly impact the ultrasonic velocity. Thus the authors
36 736 demonstrated that the temperature effect could be compensated for, but as a result, the electrolyte
37 737 temperature will require constant monitoring for this technique to be effective. Zang and co-workers
38 738 demonstrated in a follow-up study that the acoustic attenuation coefficient is a more robust parameter for
39 739 SoC monitoring. By monitoring the acoustic attenuation coefficient rather than the wave velocity, the
40 740 influence of temperature could be significantly reduced and could practically be considered negligible for
41 741 the typical 20–39°C temperature range at which VRFBs operate [129]. They showed that for the parameters
42 742 used in the study, the acoustic coefficient is most influenced by molecular relaxation processes that are
43 743 dependent on the ratio and concentration of different redox ions present in the electrolyte. They also
44 744 reported operando testing of ultrasonic SoC monitoring. They found good agreement between the acoustic
45
46
47
48
49
50
51
52
53
54
55
56
57
58
59
60

1
2
3 745 measurements and the chemical titration and inductively coupled plasma analysis with a maximum reported
4 746 deviation of 4.8%.

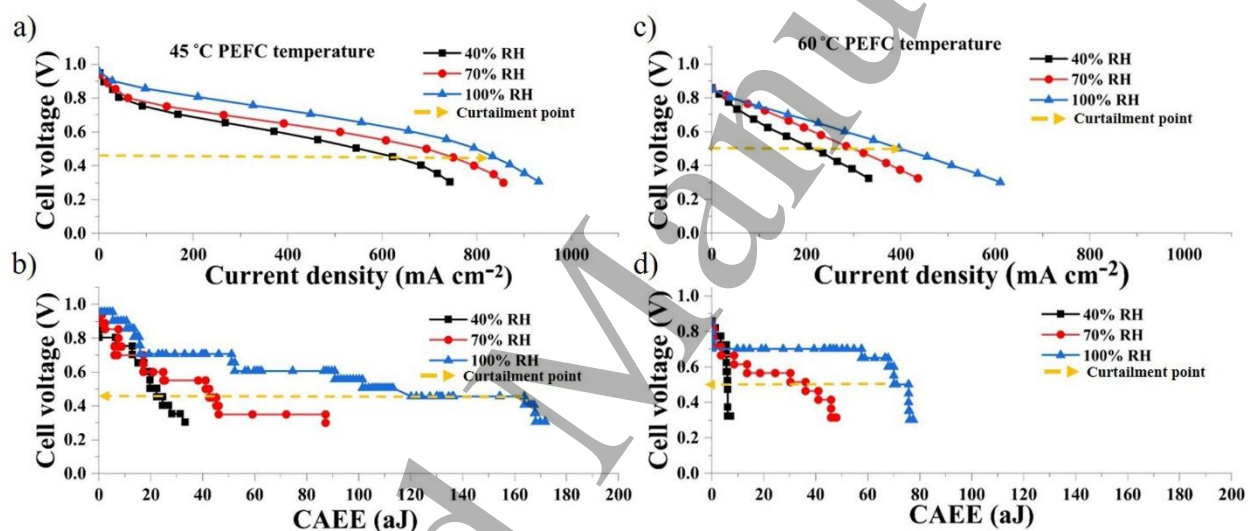
8 747 **3.3 Acoustic Characterisation of Fuel Cells**

9 748 For more reliable and high-performance PEM fuel cell and broader adoption, one major technical challenge
10 749 that must be surmounted is the water management within the cell. [130]. A minimum amount of water is
11 750 essential to keep the PEM well hydrated for good ionic conductivity. However, too much water causes
12 751 flooding in the cell, where the pores in the electrodes are filled with water, and the transport of reactant
13 752 gases to the catalyst site is obstructed [131]. Therefore, improving or optimising water management during
14 753 cell operation is crucial and has attracted significant interests [22,32,132,133].

15 754
16 755 Several techniques [37] have been employed to estimate the amount of water contained in the membrane.
17 756 However, real-time non-invasive diagnosis remains an imperative objective, and the acoustic technique has
18 757 been shown to have the potential to fill this gap. The Nafion membrane structure depends on its water
19 758 content [134], and thus its evolution gives rise to considerable structural changes. The cyclic stress and
20 759 dimensional change induced by water uptake can be substantial and are the leading causes of the mechanical
21 760 degradation of the membrane [135], which can trigger AE events.

22 761
23 762 Thus the AE technique has been applied for PEMFC diagnostics, including the water uptake of Nafion
24 763 membrane, the impact of water content on the dimensional changes occurring in a membrane [31,136], and
25 764 performance diagnosis of a PEMFC under various operating conditions [29,137]. Legros *et al.* [29,31,136]
26 765 were the first to apply the AE technique through a series of studies for water management diagnostics in
27 766 PEMFC. In their earliest study [136], they investigated the AE activity of Nafion membrane under
28 767 dehydration in a climatic chamber. The results demonstrated that the structural changes occurring in the
29 768 membrane during drying trigger AE events that can be sensed by an appropriate sensor. They further
30 769 demonstrated a relationship between the ionic conductivity of the membrane and the AE activity of the
31 770 PEMFC. They reported that the AE technique is more sensitive to the membrane dehydration process than
32 771 electrochemical impedance spectroscopy. In a subsequent study [29], the authors employed the AE
33 772 technique to investigate PEMFC under various operating conditions, such as with the membrane electrode
34 773 assembly (MEA) at open circuit and under load, and for a cell without MEA. AE events from various
35 774 sources within the cell were identified, and a strong correlation between the AE hits and the various
36 775 physicochemical phenomena taking place during cell operation was detected. They showed that the
37 776 hydrodynamics in the flow-field channels, water uptake and release by the MEA, and electrochemical
38 777 reactions could contribute to acoustic emission from the cell. Subsequently, Bethapudi *et al.* [30] used the

778 AE technique to explore fuel cell operation over a range of current densities, reactant relative humidity (RH) and cell operating temperature. The acoustic events were measured as CAEE of the acoustic hits
 779 (RH) and cell operating temperature. The acoustic events were measured as CAEE of the acoustic hits
 780 generated at discrete points of fuel cell polarisation. As shown in Figure 16, strong correlation between the
 781 PEMFC and acoustic activity were observed over the various operating conditions. The AE technique
 782 identified various features such as membrane dehydration, liquid water formation and the transition from
 783 wet channels to dry channel during operation. In a follow-up study, Bethapudi *et al.* [137] used the AE
 784 technique to evaluate hydration conditions inside PEMFC equipped with fractal flow-fields. The occurrence
 785 of flooding in the cell was shown to correspond to higher acoustic activity, further corroborated by other
 786 technique such as polarization curve and impedance spectroscopy.
 787



788
 789 **Figure 16. Correlation of PEMFC performance with acoustic activity. Top row: Polarisation curve at 40%, 70% and 100%**
 790 **reactant RH, at 45 °C and 60 °C cell temperature respectively. Bottom row: Corresponding acoustic emission CAEE at the**
 791 **various operating conditions [30].**

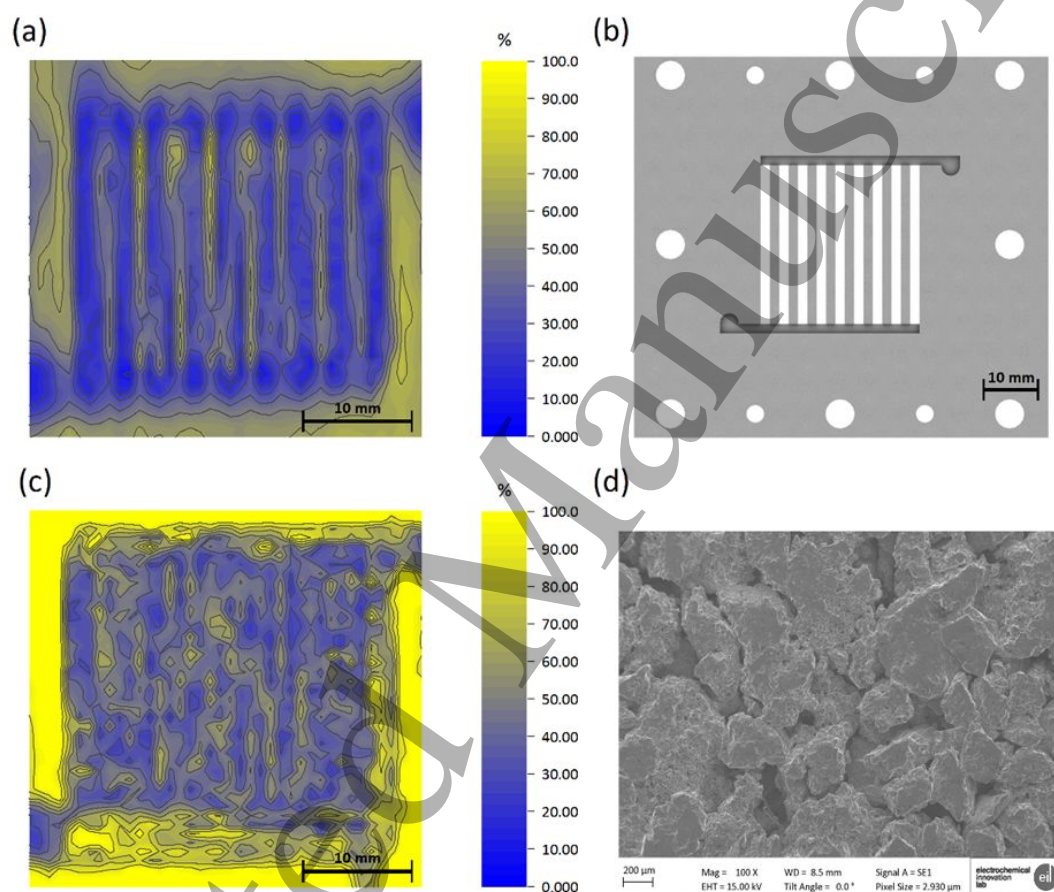
792
 793 In SOFCs, the high temperatures and reductive/oxidative environment subject the materials to significant
 794 stresses resulting in material fracturing and cracking. This mechanical stability and reliability is a critical
 795 issue for wider deployment, and the acoustic emission is ideally suited to detecting these failure
 796 mechanisms. Several studies have also used the AE technique for diagnostics of SOFCs. Bodhayan *et al.*
 797 [138] used the AE for compression testing to examine the formation of damage in SOFCs. Malzbender and
 798 Steinbrech [139] used the AE technique to monitor thermal and re-oxidation cycling to provide valuable
 799 information on mechanical stack failure mechanisms and showed AE to be a powerful tool for accessing
 800 localization of damage. Sato *et al.* [140,141] subjected a SOFC to simulated operating conditions with
 801 operando AE monitoring. They detected damage occurring within the cell, with most acoustic hits detected
 802 in the two heating periods where chemical expansion-induced stresses were highest. Three distinct types of

1
2
3 803 acoustic hits were identified based on their time lag, frequency and waveform attributed to vertical cracking
4 804 and delamination in the cathode and vertical cracking in the electrolyte. Fukui *et al.* developed an artificial
5
6 805 neural network model to produce cluster maps of acoustic events, revealing six phases of damage progress.
7
8 806 Komagata *et al.* [106] expanded on this work in a later study, using the AE technique to monitor mechanical
9
10 807 damage and deformation in a SOFC stack rather than a single cell. In addition to the mechanical damage
11
12 808 occurring in the electrodes and electrolyte, additional hits due to the deformation of stack and the friction
13
14 809 or delamination in the power collector were also observed. Recently, Rangel-Hernandez and co-workers
15
16 810 [142] used the AE technique to monitor the fracture process in the glass-ceramic material often used as a
17
18 811 sealant in SOFCs. They demonstrated the ability of AE to track the mechanical degradation of the material
19
20 812 and ascribed acoustic hits for the debonding and pull out of fibres within the structure as well as the
21
22 813 microscopic fracture of the fibres and materials found within the composite. Kumada *et al.*[143]
23
24 814 distinguished between the AE hits received as the seal cracked and damaged occurring within the cell as it
25
26 815 operated. They studied the electrochemical oxidation of the anode and found that while no hits were
27
28 816 detected for the cell operating under normal conditions under an H₂ cut-off test, vertical cracking and
29
30 817 delamination in the cell could be detected. While we did not identify any reports of the use of ToF acoustic
31
32 818 methods on SOFC, the technique would potentially identify the formation of cracks and delamination of
33
34 819 the anode/cathode layers, which can occur during start-up and shutdown. In addition, the use of ToF tools
35
36 820 will likely result in increased signal sensitivity and reliability over AE techniques due to the noise imparted
37
38 821 by the furnaces and balance-of-plant required to operate SOFCs at elevated temperatures.

34 822 **3.4 Acoustics diagnostics in PEMWEs**

36 823 In water electrolysis, degradation and two-phase water-gas management in PEMWEs are suited to non-
37
38 824 invasive diagnostics using acoustic methods. The earliest study by Crowther *et al.* [144] used the AE
39
40 825 technique to monitor gas evolution at the electrodes in an alkaline electrolyser. The authors reported an
41
42 826 increase in acoustic emission intensity with increasing gas bubble emission. More recently, Maier *et al.*
43
44 827 [145] used the AE technique to characterise the two-phase flow conditions in a single-channel PEMWE
45
46 828 cell between 0.0 A cm⁻² and 2.0 A cm⁻². During operation, the number of acoustic hits was shown to reach
47
48 829 a maximum around 0.5 A cm⁻² before decreasing to a plateau at higher current densities linked to the
49
50 830 number of gas bubbles passing the sensor in the flow channel. The average frequency of the hits also
51
52 831 decreases with current density, attributed to an increase in average bubble size which was confirmed by
53
54 832 extracting the average bubble size from high-speed optical imaging. The study showed strong correlations
55
56 833 between the water flow rates, current density and the acoustic parameters, indicating that the AE technique
57
58 834 can be used to detect the transitions from bubbly to slug flow in PEMWEs. Maier *et al.*[146] further
59
60 835 combined the AE technique with high-speed imaging to diagnose the blockage of flow channels in

1
2
3 836 PEMWEs with stagnant gas bubbles, reporting sudden step-like changes in the number of acoustic
4 837 parameters attributed to the growth of stagnant bubbles towards the AE sensor. The authors also applied
5 838 the UT technique to investigate the water-gas distribution in the flow-fields and liquid-gas diffusion layers
6 839 (LGDL) of a PEMWE during operation (Figure 17)[147]. The ultrasonic acoustic response showed a close
7 840 correlation between the acoustic attenuation in the flow-field and the production and removal of oxygen
8 841 gas through the flow channel and between the acoustic response and water thickness in the LGDL.



842
843 **Figure 17.** (a) Ultrasonic ToF scan of the anode flow-field of a PEMWE, showing rib and channel areas, as well as water
844 inlet and outlet. (b) CAD design of the flow-field, shown for comparison. (c) Ultrasonic ToF scan of the LGDL, illustrating
845 a granular distribution of high and low reflection intensity. (d) SEM image of the LGDL microstructure given for
846 comparison. Both ToF area scans were obtained during the operation of the PEMWE at a constant current density of 0.25
847 A cm⁻². Hence, water was circulated through the flow-field, and LGDL and flow channels contained water as well as oxygen
848 [147].

849 4.0 Perspective and Outlook

850 Recent advances have demonstrated the potential of the acoustic methods for diagnostics of processes,
851 degradation and health monitoring of energy conversion and power devices. Here the outlook for further
852 development and application of these techniques as well as promising future directions are discussed.

853
 854 Despite the promising developments, there is still significant scope for further application of the acoustic
 855 methods for battery diagnostics, even as the importance of battery degradation and failure monitoring
 856 increases over the coming years as batteries are placed in progressively challenging applications. Also, the
 857 desire to improve the range and reduce the cost of electric vehicle batteries drastically provides a compelling
 858 case for the manufacture of increasingly power and energy-dense packs. Furthermore, the deployment of
 859 fully electrified flight, either in the form of vertical take-off and landing or short-medium range flight, will
 860 necessitate the manufacture of batteries with energy density over 400 Wh kg⁻¹ although the viability of Li-
 861 ion technology for this application is still to be proved [74]. These various drivers will result in an increased
 862 thermal load on cells and substantially enhanced stress on the electrodes as LIBs are pushed further towards
 863 their ultimate limits. Therefore, in addition to earlier studies, there remains much room to deploy the
 864 acoustic techniques for monitoring the propagation and development of the most significant degradation
 865 pathways which have been reported in Li-ion cells. This range of possibilities is presented in Table 1
 866 [41,75–77].

867
 868 **Table 1: A summary of the potential application of acoustic techniques for monitoring of specific degradation**
 869 **mechanisms in Li-ion batteries.**

Degradation Mechanism	Cause	Effect	Potential Acoustic Signatures	Difficulty of Identification
Delamination	Electrode expansion over time, electrode cracking, manufacturing defects	Additional interface	Additional interfaces, loss of acoustic signal (if void does not contain electrolyte)	Low
Penetration	Insertion of foreign body	Distortion of layers, presence of additional interfaces, temperature rise, gas generation	Change in overall waveform, presence of additional layers, increased acoustic impedance	Low
Internal short circuit	Foreign body, failure of separator	Gas generation, temperature rise	Loss of signal, increased acoustic impedance, change in overall waveform	Low
Thermal Runaway	Electrolyte/electrode reaction	Severe gas generation, electrode movement, temperature rise	Loss of signal, increased acoustic impedance, change in overall waveform	Low

Electrolyte decomposition	Li reaction with electrolyte	Reduced capacity/power	Reduced transmission between layers	Medium
Porosity change	Electrode swelling, SEI formation	Change in mechanical properties of electrode	Change in acoustic impedance, speed of sound, change in ToF of peaks	Medium
Current collector corrosion	Electrolyte reaction, potential outside safe range	Change in composition of current collector, additional interface	Altered speed of sound, change in ToF of peaks	Medium
Li-plating	Low temperature operation, high rate operation, heterogenous current distribution	Formation of Li layer, gas generation	Increased acoustic impedance, additional interface, change in ToF of peaks	Medium
Metal oxide degradation	Phase and structural changes	Change in mechanical properties of electrode	Change in acoustic impedance, enhanced stress-strain effects	Medium
Metal dissolution	Reaction with electrolyte	Change in mechanical properties of electrode	Change in acoustic impedance, enhanced stress-strain effects	Medium/High
Dislocation of particles	Binder decomposition, electrode swelling	Change in electrode density	Altered speed of sound, change in ToF of peaks	Medium/High
SEI growth reducing surface area	Electrolyte reaction with electrodes	Additional interface, gas generation	Additional interface, reduced transmission	Medium/High
Decomposition of binder	Reaction with charged anode to form LiF	Loss of connected material	Altered speed of sound, change in ToF of peaks	Medium/High
Particle cracking	Electrode swelling	Change in electrode density	Change in speed of sound, change in ToF of peaks	Medium/High

870
871 Acoustic techniques also offer the possibility to provide near real-time information to battery management
872 systems due to the short measurement durations. Therefore, tracking of degradation and failure of cells can
873 be achieved over the cell lifetime in several ways. In the simplest BMS integration, a simple fault signal
874 could be delivered if a characteristic event is observed [35]. In contrast to electrical measurements, this
875 signal is related to the mechanical structure of the cells, providing a secondary means of monitoring the
876 safety of battery systems. Further, acoustic signals could be supplied to a reduced-order model to enable an
877 alternative method for degradation monitoring and frequency analysis could be performed to correlate a
878 signal to specific depths and identify degradation at locations within battery packs [85]. The comparatively

1
2
3 879 low cost, compact, lightweight nature of acoustic techniques will enable the widespread deployment of this
4 880 tool in battery technology and could complement existing monitoring technology, including thermal and
5 881 electrochemical measurements to extend the lifetime of batteries.
6
7

8 882

9 883 Acoustic techniques also offer the potential to screen cells that have reached the end of their useable first
10 884 life, often considered to be 80% of initial SoC. Given the existing challenges with Li-ion battery recycling
11 885 [86], there is an increasing drive to reuse or repurpose batteries, focusing on domestic storage and
12 886 applications in developing economies [87,88]. To achieve this on a massive scale, the rapid assessment of
13 887 the SoH of the cell is imperative. Thus, the acoustic methods are amongst the most promising techniques
14 888 due to their rapid acquisition time. Here the acoustic methods could be used to probe the cell, which are
15 889 then categorized against a predefined pass/fail criteria. In this scenario, failed cells could be subjected to
16 890 further analysis. The screening process could also be extended to the manufacturing of new cells, in which
17 891 acoustic tools act as part of a triage system, enabling cells that do not pass criteria to be examined using a
18 892 secondary technique that can assess the extent of the defect in more detail, before a decision on the
19 893 suitability of the cell is made. To enable the deployment of acoustic tools in these various scenarios,
20 894 substantial developments will be required, especially in the analysis of cylindrical cells, which, to date,
21 895 have not been well characterised due to the challenges posed by their geometry.
22
23
24
25
26
27
28
29

30 896

31 897 Beyond Li-ion chemistry, there exists an opportunity to develop diagnostic and monitoring techniques in
32 898 concert with novel battery types. Cells containing a Li-metal anode are at an advanced stage of
33 899 development, with an expectation that such cells will replace Li-ion in specific niche applications by the
34 900 end of the decade [89]. These cells are challenging to image using conventional X-ray techniques due to
35 901 the low attenuation of Li metal, offering an opportunity for acoustic imaging to aid their developments.
36 902 Indeed, the delamination of electrodes in solid-state batteries, which have the potential for enhanced
37 903 volumetric energy density, could be monitored using acoustic methods in a relatively facile manner. Na-
38 904 ion cells that may be used as a low-cost alternative to LIBs in low power scenarios also offer significant
39 905 potential for acoustic analysis. These cells contain similar components to LIBs will allow a straightforward
40 906 migration of acoustic techniques to these cells should become widely adopted. Li-S batteries offer
41 907 substantial improvements in gravimetric energy density and are particularly well suited to acoustic
42 908 monitoring. The large changes in the density of the cathode and viscosity of the electrolyte provide the
43 909 opportunity to monitor the SoH and SoC of these cells in a manner which is challenging using
44 910 electrochemical methods due to the tendency of the cells to relax to an open-circuit voltage in the middle
45 911 of the operating window [148]. Also, monitoring the 'polysulfide shuttle effect' as well as characterisation
46 912 of the optimum storage conditions for particular cells could be possible using these tools. As most of these
47
48
49
50
51
52
53
54
55
56
57
58
59
60

Degradation Mechanism	Cause	Effect	Potential Acoustic Signatures	Difficulty of Identification	Ref.
Electrode delamination	Poor adhesion to membrane	Reduction in active catalytic sites	Additional interfaces, loss of acoustic signal	Low	[149]
Blocking of catalytic sites (FC)	Flooding/excess water content in cell	Heterogeneous current density/thermal distribution in cell	Increased transmission through cell	Low	[150]
Gas diffusion layer cracking	Excessive compression, low temperature operation	Inhibited electrical contact, inhomogeneous thermal distribution	Additional interfaces, loss of signal across cell	Low	[151]
Bipolar plate corrosion	High humidity, acidity of operating environment	Loss of electrical contact, potential catalyst poisoning	Loss of interface, decreased transmission through cell	Low	[152]
Bipolar plate fracture	Excessive compression, cold start/low temperature	Inhibited electrical contact, inhomogeneous thermal	Additional interfaces, loss of signal across cell	Low	[153]

913 battery types and chemistries are in a comparatively early stage of commercialisation, there remains an
 914 opportunity to develop a suite of diagnostic tools in which the acoustic methods could play a huge role [90].

915 4.2 Perspectives for Fuel cells and Water Electrolysers

916 Passive acoustic techniques have offered significant benefit for monitoring both water formation and
 917 membrane cracking in PEMFC and are expected to continue to provide a useful diagnosis for water
 918 management. However, possibilities abound for the deployment of the acoustic methods during cell design
 919 and manufacturing, especially in SOFCs where thermal considerations are paramount. As initial studies
 920 have shown, the multi-layered ceramic geometry of SOFCs can be monitored using acoustic methods to
 921 ensure the integrity of the device. In water electrolysis, a handful of studies have shown the significant
 922 potential of the acoustic techniques for PEMWE diagnostics, particularly to study two-phase flow and mass
 923 transport processes during system operation with much room for further deployment for understanding
 924 degradation in cell components for cell performance optimization. Table 2 highlights the various
 925 possibilities for the deployment of the acoustic methods for diagnostics of critical design and process
 926 parameters in both fuel cell and electrolyser technologies.

927
 928 **Table 2. A summary of potential applications of acoustic techniques for monitoring of specific process and degradation in**
 929 **fuel cells and electrolysers.**

	operation	distribution			
Mismatched electrodes	Substandard manufacturing	Poor electrical contact, gas leaking	Poor transmission across cell, spatially variant interfaces	Low	[154]
Poor contact	Insufficient compression	Poor electrical contact, excessive Ohmic heating	Poor transmission across cell	Low	[155]
Membrane dehydration	High temperature and high rate operation	Decrease in membrane malleability	Reduced transmission across cell	Low/Medium	[156]
Fouling/particulate build-up (Electrolyser)	Dissolved solids in liquid streams, corrosion of pipes	Blocking of flow channels	Additional interfaces	Low/Medium	[86]
Seal failure	Degradation of component material, high pressure	Gas leaking, stack failure	Poor transmission across cell, additional interfaces	Medium	[157]
Blocking of catalytic sites (Electrolyser)	Excess gas in cell	Heterogeneous current density, enhanced stress on membrane	Decreased transmission through cell	Medium	[158]
Catalyst layer cracking	Migration of catalytic particles, excessive compression	Dislocation of active catalytic sites	Additional interfaces, loss of signal across cell	Medium	[159]
Fouling/particulate build up (FC)	Particulates in gas streams, corrosion of pipes, of particular concern in microbial fuel cells	Blocking of gas channels	Additional interfaces, increased transmission through cell	Medium	[160]
Pinhole formation	High temperature and high rate operation	Increase in membrane dehydration locally	Loss of and/or reduction in signal	Medium/High	[161]
Catalyst poisoning	Interaction with bipolar plates	Heterogeneous current density	Reduced transmission at bipolar plate	High	[162]

930

931 5.0 Conclusion

932 This review discusses recent progress in the increasing application of acoustic methods for process
 933 diagnostics and health monitoring of various electrochemical power devices. The fundamental principle

1
2
3 934 and theory behind the acoustic emission and ultrasonic testing techniques and its suitability to diagnostic
4 935 of electrochemical devices are discussed, and the various implementation of the acoustic techniques in
5 936 various electrochemical power systems highlighted. Perspectives on future applications for this technique
6 937 are provided for both battery and polymer electrolyte devices with a focus on identifying specific
7 938 degradation and failure modes.

8 939
9
10
11 940 Across the range of devices reviewed, it can be seen that the physical, chemical, and mechanical changes
12 941 during the operation of these electrochemical power devices can be detected using AE features, especially
13 942 amplitude, frequency, counts and cumulative acoustic energy. In battery applications, many researchers
14 943 found that electrode particle cracking and gas evolution by electrolyte decomposition are the main sources
15 944 of acoustic emission in batteries. In ultrasonic testing of batteries, various processes and degradation were
16 945 detected as a shift in amplitude and time of flight of acoustic signal. Given the high rate of publication in
17 946 this area it is anticipated that acoustic techniques will play an increasing role in the diagnosis of degradation
18 947 and failure mechanisms in the years to come. There is also a clear scope to deploy these techniques in the
19 948 development of reuse and recycling efforts which will become increasingly important as the volume of used
20 949 cells increases with the replacement of the early fleet of electric vehicles.

21 950
22 951 While both AE and UT techniques have also been deployed in fuel cells and electrolysers, the number of
23 952 reports is significantly smaller. These have primarily focussed on the study of two-phase transport, water
24 953 management and cell degradation, however it is clear that there remains a wide range of uses for acoustic
25 954 methods which have yet to be explored in these fields in particular at the stack level, at which acoustic tools
26 955 offer substantial benefits over more invasive techniques. It is expected that the acoustic techniques will
27 956 form a key part of the diagnostic tools for monitoring electrochemical devices across various processes
28 957 including fabrication, *operando* and *post mortem* diagnostics and in the end-of-life decision making
29 958 process.

30 959 **Acknowledgements**

31 960 The authors would like to gratefully acknowledge the EPSRC for supporting the electrochemical research
32 961 in the Electrochemical Innovation Lab (EP/R020973/1; EP/R023581/1; EP/N032888/1; EP/R023581/1;
33 962 EP/P009050/1; EP/M014371/1; EP/M009394; EP/L015749/1, EP/K038656/1) and Innovate UK for
34 963 funding the VALUABLE project (Grant No. 104182). The authors would also like to acknowledge the
35 964 Royal Academy of Engineering for funding Robinson and Shearing through ICRF1718\1\34 and CiET1718
36 965 respectively and the Faraday Institution (EP/S00353/1, grants FIRG003, FIRG014). The authors also
37 966 acknowledge the STFC for supporting Shearing and Brett (ST/K00171X/1) and ACEA for supporting

1
2
3 967 ongoing research at the EIL. Support from the National Measurement System of the UK Department for
4 968 Business, Energy and Industrial Strategy is also gratefully acknowledged.

5
6 969

7
8 970 **References**

- 9 971 [1] REN 21 - RENEWABLES NOW. Renewables 2019 - Global Status Report. 2019.
10 972 <https://doi.org/10.3390/resources8030139>.
- 11 973 [2] Barbir F. PEM electrolysis for production of hydrogen from renewable energy sources. *Sol Energy*
12 974 2005;78:661–9. <https://doi.org/10.1016/j.solener.2004.09.003>.
- 13 975 [3] Yang Y, Yuan W, Zhang X, Yuan Y, Wang C, Ye Y, et al. Overview on the applications of three-
14 976 dimensional printing for rechargeable lithium-ion batteries. *Appl Energy* 2020;257:114002.
15 977 <https://doi.org/10.1016/J.APENERGY.2019.114002>.
- 16 978 [4] Larcher D, Tarascon JM. Towards greener and more sustainable batteries for electrical energy
17 979 storage. *Nat Chem* 2015. <https://doi.org/10.1038/nchem.2085>.
- 18 980 [5] Scrosati B, Garche J. Lithium batteries: Status, prospects and future. *J Power Sources* 2010.
19 981 <https://doi.org/10.1016/j.jpowsour.2009.11.048>.
- 20 982 [6] Clarke RE, Giddey S, Ciacchi FT, Badwal SPS, Paul B, Andrews J. Direct coupling of an
21 983 electrolyser to a solar PV system for generating hydrogen. *Int J Hydrogen Energy* 2009;34:2531–
22 984 42. <https://doi.org/10.1016/j.ijhydene.2009.01.053>.
- 23 985 [7] Chen K, Jiang SP. Review—Materials Degradation of Solid Oxide Electrolysis Cells. *J*
24 986 *Electrochem Soc* 2016. <https://doi.org/10.1149/2.0101611jes>.
- 25 987 [8] Taiwo OO, Heenan TMM, Finegan DP, Brett DJL, Shearing PR, Paz-García JM, et al.
26 988 Microstructural degradation of silicon electrodes during lithiation observed via operando X-ray
27 989 tomographic imaging. *J Power Sources* 2017. <https://doi.org/10.1016/j.jpowsour.2016.12.070>.
- 28 990 [9] Yoo HD, Markevich E, Salitra G, Sharon D, Aurbach D. On the challenge of developing advanced
29 991 technologies for electrochemical energy storage and conversion. *Mater Today* 2014.
30 992 <https://doi.org/10.1016/j.mattod.2014.02.014>.
- 31 993 [10] Yuan XZ, Song C, Platt A, Zhao N, Wang H, Li H, et al. A review of all-vanadium redox flow
32 994 battery durability: Degradation mechanisms and mitigation strategies. *Int J Energy Res* 2019.
33 995 <https://doi.org/10.1002/er.4607>.
- 34 996 [11] Wang W, Luo Q, Li B, Wei X, Li L, Yang Z. Recent progress in redox flow battery research and
35 997 development. *Adv Funct Mater* 2013. <https://doi.org/10.1002/adfm.201200694>.
- 36 998 [12] Kulkarni N, Kok MDR, Jervis R, Iacoviello F, Meyer Q, Shearing PR, et al. The effect of non-
37 999 uniform compression and flow-field arrangements on membrane electrode assemblies - X-ray
38 1000 computed tomography characterisation and effective parameter determination. *J Power Sources*

- 1
2
3 1001 2019. <https://doi.org/10.1016/j.jpowsour.2019.04.018>.
- 4
5 1002 [13] Wang Y, Chen KS, Mishler J, Cho SC, Adroher XC. A review of polymer electrolyte membrane
6 1003 fuel cells: Technology, applications, and needs on fundamental research. *Appl Energy* 2011.
7
8 1004 <https://doi.org/10.1016/j.apenergy.2010.09.030>.
- 9
10 1005 [14] Choudhury A, Chandra H, Arora A. Application of solid oxide fuel cell technology for power
11 1006 generation - A review. *Renew Sustain Energy Rev* 2013.
12
13 1007 <https://doi.org/10.1016/j.rser.2012.11.031>.
- 14 1008 [15] Dmitri B, Wang H, Hui L, Zhao N, editors. *PEM Electrolysis for Hydrogen Production: Principles*
15 1009 *and Applications*. 1st ed. CRC Press; 2016.
- 16
17 1010 [16] Liu C, Li F, Lai-Peng M, Cheng HM. *Advanced materials for energy storage*. *Adv Mater* 2010.
18
19 1011 <https://doi.org/10.1002/adma.200903328>.
- 20
21 1012 [17] Alotto P, Guarnieri M, Moro F. Redox flow batteries for the storage of renewable energy: A
22 1013 review. *Renew Sustain Energy Rev* 2014;29:325–35. <https://doi.org/10.1016/j.rser.2013.08.001>.
- 23
24 1014 [18] Barbir F. *PEM Fuel Cells*. 2005. <https://doi.org/10.1016/B978-0-12-078142-3.X5000-9>.
- 25
26 1015 [19] Borup R, Meyers J, Pivovar B, Kim YS, Mukundan R, Garland N, et al. Scientific aspects of
27 1016 polymer electrolyte fuel cell durability and degradation. *Chem Rev* 2007.
28
29 1017 <https://doi.org/10.1021/cr050182l>.
- 30 1018 [20] Rabis A, Rodriguez P, Schmidt TJ. Electrocatalysis for polymer electrolyte fuel cells: Recent
31 1019 achievements and future challenges. *ACS Catal* 2012. <https://doi.org/10.1021/cs3000864>.
- 32
33 1020 [21] Hou J, Yang M, Zhang J. Active and passive fuel recirculation for solid oxide and proton
34 1021 exchange membrane fuel cells. *Renew Energy* 2020. <https://doi.org/10.1016/j.renene.2020.04.002>.
- 35
36 1022 [22] Cho JIS, Neville TP, Trogadas P, Bailey J, Shearing P, Brett DJL, et al. Capillaries for water
37 1023 management in polymer electrolyte membrane fuel cells. *Int J Hydrogen Energy* 2018;43:21949–
38 1024 58. <https://doi.org/10.1016/j.ijhydene.2018.10.030>.
- 39
40 1025 [23] da Silva FS, de Souza TM. Novel materials for solid oxide fuel cell technologies: A literature
41 1026 review. *Int J Hydrogen Energy* 2017. <https://doi.org/10.1016/j.ijhydene.2017.08.105>.
- 42
43 1027 [24] Lu X, Heenan TMM, Bailey JJ, Li T, Li K, Brett DJL, et al. Correlation between triple phase
44 1028 boundary and the microstructure of Solid Oxide Fuel Cell anodes: The role of composition,
45 1029 porosity and Ni densification. *J Power Sources* 2017.
46
47 1030 <https://doi.org/10.1016/j.jpowsour.2017.08.095>.
- 48
49 1031 [25] Carmo M, Fritz DL, Mergel J, Stolten D. A comprehensive review on PEM water electrolysis. *Int*
50 1032 *J Hydrogen Energy* 2013;38:4901–34. <https://doi.org/10.1016/j.ijhydene.2013.01.151>.
- 51
52 1033 [26] Rezvanizani SM, Liu Z, Chen Y, Lee J. Review and recent advances in battery health
53 1034 monitoring and prognostics technologies for electric vehicle (EV) safety and mobility. *J Power*

- 1
2
3 1035 Sources 2014. <https://doi.org/10.1016/j.jpowsour.2014.01.085>.
- 4
5 1036 [27] Berecibar M, Gandiaga I, Villarreal I, Omar N, Van Mierlo J, Van Den Bossche P. Critical review
6 1037 of state of health estimation methods of Li-ion batteries for real applications. *Renew Sustain*
7 1038 *Energy Rev* 2016. <https://doi.org/10.1016/j.rser.2015.11.042>.
- 8
9 1039 [28] Zang X, Yan L, Yang Y, Pan H, Nie Z, Jung KW, et al. Monitoring the State-of-Charge of a
10 1040 Vanadium Redox Flow Battery with the Acoustic Attenuation Coefficient: An In Operando
11 1041 Noninvasive Method. *Small Methods* 2019. <https://doi.org/10.1002/smt.201900494>.
- 12
13 1042 [29] Legros B, Thivel PX, Bultel Y, Boinet M, Nogueira RP. Acoustic emission: Towards a real-time
14 1043 diagnosis technique for Proton exchange membrane fuel cell operation. *J Power Sources*
15 1044 2010;195:8124–33. <https://doi.org/10.1016/j.jpowsour.2010.07.045>.
- 16
17 1045 [30] Bethapudi VS, Maier M, Hinds G, Shearing PR, Brett DJL, Coppens MO. Acoustic emission as a
18 1046 function of polarisation: Diagnosis of polymer electrolyte fuel cell hydration state. *Electrochem*
19 1047 *Commun* 2019;109:106582. <https://doi.org/10.1016/j.elecom.2019.106582>.
- 20
21 1048 [31] Legros B, Thivel PX, Druart F, Bultel Y, Nogueira R. Diagnosis and modelling of
22 1049 protonexchange-Membrane fuel cell via electrochemical-Impedance-Spectroscopy and acoustic-
23 1050 Emission measurements. 2009 8th Int Symp Adv Electromechanical Motion Syst Electr Drives Jt
24 1051 Symp ELECTROMOTION 2009 2009:1–3.
25 1052 <https://doi.org/10.1109/ELECTROMOTION.2009.5259133>.
- 26
27 1053 [32] Cho JIS, Neville TP, Trogadas P, Meyer Q, Wu Y, Ziesche R, et al. Visualization of liquid water
28 1054 in a lung-inspired flow-field based polymer electrolyte membrane fuel cell via neutron
29 1055 radiography. *Energy* 2019. <https://doi.org/10.1016/j.energy.2018.12.143>.
- 30
31 1056 [33] Robinson JB, Brown LD, Jervis R, Taiwo OO, Heenan TMM, Millichamp J, et al. Investigating
32 1057 the effect of thermal gradients on stress in solid oxide fuel cell anodes using combined synchrotron
33 1058 radiation and thermal imaging. *J Power Sources* 2015.
34 1059 <https://doi.org/10.1016/j.jpowsour.2015.04.104>.
- 35
36 1060 [34] Dedigama I, Angeli P, Van Dijk N, Millichamp J, Tsaoulidis D, Shearing PR, et al. Current
37 1061 density mapping and optical flow visualisation of a polymer electrolyte membrane water
38 1062 electrolyser. *J Power Sources* 2014;265:97–103. <https://doi.org/10.1016/j.jpowsour.2014.04.120>.
- 39
40 1063 [35] Majasan JO, Cho JIS, Dedigama I, Tsaoulidis D, Shearing P, Brett DJL. Two-phase flow
41 1064 behaviour and performance of polymer electrolyte membrane electrolysers: Electrochemical and
42 1065 optical characterisation. *Int J Hydrogen Energy* 2018;43.
43 1066 <https://doi.org/10.1016/j.ijhydene.2018.07.003>.
- 44
45 1067 [36] Birkel CR, Roberts MR, McTurk E, Bruce PG, Howey DA. Degradation diagnostics for lithium ion
46 1068 cells. *J Power Sources* 2017. <https://doi.org/10.1016/j.jpowsour.2016.12.011>.
- 47
48
49
50
51
52
53
54
55
56
57
58
59
60

- 1
2
3 1069 [37] Wu J, Yuan XZ, Wang H, Blanco M, Martin JJ, Zhang J. Diagnostic tools in PEM fuel cell
4 1070 research: Part I Electrochemical techniques. *Int J Hydrogen Energy* 2008;33:1735–46.
5 1071 <https://doi.org/10.1016/j.ijhydene.2008.01.013>.
6
7
8 1072 [38] Lu J, Wu T, Amine K. State-of-the-art characterization techniques for advanced lithium-ion
9 1073 batteries. *Nat Energy* 2017. <https://doi.org/10.1038/nenergy.2017.11>.
10
11 1074 [39] Liu D, Shadik Z, Lin R, Qian K, Li H, Li K, et al. Review of Recent Development of In
12 1075 Situ/Operando Characterization Techniques for Lithium Battery Research. *Adv Mater*
13 1076 2019;31:1806620. <https://doi.org/10.1002/adma.201806620>.
14
15
16 1077 [40] Robinson JB, Shearing PR, Brett DJL. Thermal imaging of electrochemical power systems: A
17 1078 review. *J Imaging* 2016;2. <https://doi.org/10.3390/jimaging2010002>.
18
19 1079 [41] Robinson JB, Engebretsen E, Finegan DP, Darr J, Hinds G, Shearing PR, et al. Detection of
20 1080 internal defects in lithium-ion batteries using lock-in thermography. *ECS Electrochem Lett*
21 1081 2015;4:A106–9. <https://doi.org/10.1149/2.0071509eel>.
22
23
24 1082 [42] Heenan TMM, Tan C, Hack J, Brett DJL, Shearing PR. Developments in X-ray tomography
25 1083 characterization for electrochemical devices. *Mater Today* 2019.
26 1084 <https://doi.org/10.1016/j.mattod.2019.05.019>.
27
28
29 1085 [43] Ziesche RF, Robinson JB, Kok MDR, Markötter H, Kockelmann W, Kardjilov N, et al. Editors'
30 1086 Choice—4D Neutron and X-ray Tomography Studies of High Energy Density Primary Batteries:
31 1087 Part I. Dynamic Studies of LiSOCl₂ during Discharge. *J Electrochem Soc* 2020.
32 1088 <https://doi.org/10.1149/1945-7111/abbbbc>.
33
34
35 1089 [44] Wang H, Yuan XZ, Li H. PEM fuel cell diagnostic tools. 2011.
36
37 1090 [45] Tsushima S, Hirai S. In situ diagnostics for water transport in proton exchange membrane fuel
38 1091 cells. *Prog Energy Combust Sci* 2011. <https://doi.org/10.1016/j.pecs.2010.06.001>.
39
40 1092 [46] Qu D, Wang G, Kafle J, Harris J, Crain L, Jin Z, et al. Electrochemical Impedance and its
41 1093 Applications in Energy-Storage Systems. *Small Methods* 2018.
42 1094 <https://doi.org/10.1002/smt.201700342>.
43
44 1095 [47] Yuan Y, Amine K, Lu J, Shahbazian-Yassar R. Understanding materials challenges for
45 1096 rechargeable ion batteries with in situ transmission electron microscopy. *Nat Commun* 2017.
46 1097 <https://doi.org/10.1038/ncomms15806>.
47
48
49 1098 [48] Fan Z, Zhang L, Baumann D, Mei L, Yao Y, Duan X, et al. In Situ Transmission Electron
50 1099 Microscopy for Energy Materials and Devices. *Adv Mater* 2019.
51 1100 <https://doi.org/10.1002/adma.201900608>.
52
53
54 1101 [49] Mohammadi M, Jerschow A. In situ and operando magnetic resonance imaging of electrochemical
55 1102 cells: A perspective. *J Magn Reson* 2019. <https://doi.org/10.1016/j.jmr.2019.106600>.
56
57
58
59
60

- 1
2
3 1103 [50] Wang S, Liu Q, Zhao C, Lv F, Qin X, Du H, et al. Advances in Understanding Materials for
4 1104 Rechargeable Lithium Batteries by Atomic Force Microscopy. *Energy Environ Mater* 2018.
5 1105 <https://doi.org/10.1002/eem2.12002>.
6
7
8 1106 [51] Kardjilov N, Manke I, Woracek R, Hilger A, Banhart J. Advances in neutron imaging. *Mater*
9 1107 *Today* 2018. <https://doi.org/10.1016/j.mattod.2018.03.001>.
10
11 1108 [52] Selamat OF, Pasaogullari U, Spornjak D, Hussey DS, Jacobson DL, Mat MD. Two-phase flow in a
12 1109 proton exchange membrane electrolyzer visualized in situ by simultaneous neutron radiography
13 1110 and optical imaging. *Int J Hydrogen Energy* 2013;38:5823–35.
14 1111 <https://doi.org/10.1016/j.ijhydene.2013.02.087>.
15
16 1112 [53] Majasan JO, Cho JIS, Dedigama I, Tsaoulidis D, Shearing P, Brett DJL. Two-phase flow
17 1113 behaviour and performance of polymer electrolyte membrane electrolyzers: Electrochemical and
18 1114 optical characterisation. *Int J Hydrogen Energy* 2018;43:15659–72.
19 1115 <https://doi.org/10.1016/j.ijhydene.2018.07.003>.
20
21
22 1116 [54] Practical Acoustic Emission Testing. 2016. <https://doi.org/10.1007/978-4-431-55072-3>.
23
24 1117 [55] ASTM (American Society for Testing and Materials). E1316 - Standard Terminology for
25 1118 Nondestructive Examinations. *ASTM Int* 2011. <https://doi.org/10.1520/E1316-11B>.
26
27 1119 [56] Introduction to Acoustic Emission Testing. NDT Resour Cent n.d. <https://www.nde->
28 1120 [ed.org/EducationResources/CommunityCollege/OtherMethods/AE/AE_Intro.php](https://www.nde-ed.org/EducationResources/CommunityCollege/OtherMethods/AE/AE_Intro.php) (accessed
29 1121 August 25, 2020).
30
31
32 1122 [57] Schuh A, Hegyi A, Raghavan A, Lochbaum A, Schwartz J, Kiesel P. High-resolution, high-
33 1123 frequency wavelength shift detection of optical signals with low-cost, compact readouts. *Fiber*
34 1124 *Opt. Sensors Appl. XII*, 2015. <https://doi.org/10.1117/12.2177478>.
35
36
37 1125 [58] Jata K V., Kundu T, Parthasarathy TA. An Introduction to Failure Mechanisms and Ultrasonic
38 1126 Inspection. *Adv. Ultrason. Methods Mater. Struct. Insp.*, 2010.
39 1127 <https://doi.org/10.1002/9780470612248.ch1>.
40
41
42 1128 [59] Godin N, Reynaud P, Fantozzi G. Acoustic Emission: Definition and Overview. *Acoust. Emiss.*
43 1129 *Durab. Compos. Mater.*, 2018. <https://doi.org/10.1002/9781119426660.ch1>.
44
45
46 1130 [60] Lemarié Q, Alloin F, Thivel PX, Idrissi H, Roué L. Study of sulfur-based electrodes by operando
47 1131 acoustic emission. *Electrochim Acta* 2019;299:415–22.
48 1132 <https://doi.org/10.1016/j.electacta.2019.01.019>.
49
50
51 1133 [61] Nair A, Cai CS. Acoustic emission monitoring of bridges: Review and case studies. *Eng Struct*
52 1134 2010. <https://doi.org/10.1016/j.engstruct.2010.02.020>.
53
54 1135 [62] Lee DE, Hwang I, Valente CMO, Oliveira JFG, Dornfeld DA. Precision manufacturing process
55 1136 monitoring with acoustic emission. *Int J Mach Tools Manuf* 2006.

- 1
2
3 1137 <https://doi.org/10.1016/j.ijmachtools.2005.04.001>.
- 4
5 1138 [63] Jirarungsatian C, Prateepasen A. Pitting and uniform corrosion source recognition using acoustic
6 1139 emission parameters. *Corros Sci* 2010. <https://doi.org/10.1016/j.corsci.2009.09.001>.
- 7
8 1140 [64] Azumi K, Ishiguro S, Mizuno T, Seo M. Acoustic emission from a palladium electrode during
9 1141 hydrogen charging and its release in a LiOH electrolyte. *J Electroanal Chem* 1993.
10 1142 [https://doi.org/10.1016/0022-0728\(93\)80082-S](https://doi.org/10.1016/0022-0728(93)80082-S).
- 11
12 1143 [65] Jomdecha C, Prateepasen A, Kaewtrakulpong P. Study on source location using an acoustic
13 1144 emission system for various corrosion types. *NDT E Int* 2007.
14 1145 <https://doi.org/10.1016/j.ndteint.2007.05.003>.
- 15
16 1146 [66] Kim YP, Fregonese M, Mazille H, Feron D, Santarini G. Study of oxygen reduction on stainless
17 1147 steel surfaces and its contribution to acoustic emission recorded during corrosion processes.
18 1148 *Corros Sci* 2006. <https://doi.org/10.1016/j.corsci.2006.03.006>.
- 19
20 1149 [67] Sarasini F, Santulli C. Non-destructive testing (NDT) of natural fibre composites: acoustic
21 1150 emission technique n.d. <https://doi.org/10.1533/9780857099228.3.273>.
- 22
23 1151 [68] Eaton MJ, Pullin R, Holford KM. Towards improved damage location using acoustic emission.
24 1152 *Proc Inst Mech Eng Part C J Mech Eng Sci* 2012. <https://doi.org/10.1177/0954406212449582>.
- 25
26 1153 [69] Mancini S, Tumino G, Gaudenzi P. Structural health monitoring for future space vehicles. *J Intell*
27 1154 *Mater Syst Struct* 2006. <https://doi.org/10.1177/1045389X06059077>.
- 28
29 1155 [70] Saeedifar M, Saleh MN, De Freitas ST, Zarouchas D. Damage characterization of adhesively-
30 1156 bonded Bi-material joints using acoustic emission. *Compos Part B Eng* 2019.
31 1157 <https://doi.org/10.1016/j.compositesb.2019.107356>.
- 32
33 1158 [71] Noorsuhada MN. An overview on fatigue damage assessment of reinforced concrete structures
34 1159 with the aid of acoustic emission technique. *Constr Build Mater* 2016;112:424–39.
35 1160 <https://doi.org/10.1016/j.conbuildmat.2016.02.206>.
- 36
37 1161 [72] Shateri M, Ghaib M, Svecova D, Thomson D. On acoustic emission for damage detection and
38 1162 failure prediction in fiber reinforced polymer rods using pattern recognition analysis. *Smart Mater*
39 1163 *Struct* 2017. <https://doi.org/10.1088/1361-665X/aa6e43>.
- 40
41 1164 [73] Czichos H. Handbook of technical diagnostics: fundamentals and application to structures and
42 1165 systems. 2013.
- 43
44 1166 [74] Ensminger D, Bond LJ. *Ultrasonics: Fundamentals, technologies, and applications*, third edition.
45 1167 2011.
- 46
47 1168 [75] Davies G, Knehr KW, Van Tassell B, Hodson T, Biswas S, Hsieh AG, et al. State of Charge and
48 1169 State of Health Estimation Using Electrochemical Acoustic Time of Flight Analysis. *J*
49 1170 *Electrochem Soc* 2017;164:A2746–55. <https://doi.org/10.1149/2.1411712jes>.
- 50
51
52
53
54
55
56
57
58
59
60

- 1
2
3 1171 [76] Robinson JB, Pham M, Kok MDR, Heenan TMM, Brett DJL, Shearing PR. Examining the
4 1172 Cycling Behaviour of Li-Ion Batteries Using Ultrasonic Time-of-Flight Measurements. *J Power*
5 1173 *Sources* 2019;444:227318. <https://doi.org/10.1016/j.jpowsour.2019.227318>.
6
7 1174 [77] Kundu T, Placko D. *Advanced Ultrasonic Methods for Material and Structure Inspection*. 2010.
8 1175 <https://doi.org/10.1002/9780470612248>.
9
10 1176 [78] Robinson JB, Owen RE, Kok MDR, Maier M, Majasan J, Braglia M, et al. Identifying Defects in
11 1177 Li-Ion Cells Using Ultrasound Acoustic Measurements. *J Electrochem Soc* 2020;167:120530.
12 1178 <https://doi.org/10.1149/1945-7111/abb174>.
13
14 1179 [79] Wu Y, Wang Y, Yung WKC, Pecht M. Ultrasonic Health Monitoring of Lithium-Ion Batteries.
15 1180 *Electronics* 2019;8:751. <https://doi.org/10.3390/electronics8070751>.
16
17 1181 [80] Bommier C, Chang W, Li J, Biswas S, Davies G, Nanda J, et al. Operando Acoustic Monitoring of
18 1182 SEI Formation and Long-Term Cycling in NMC/SiGr Composite Pouch Cells. *J Electrochem Soc*
19 1183 2020;167:020517. <https://doi.org/10.1149/1945-7111/ab68d6>.
20
21 1184 [81] Nitta N, Wu F, Lee JT, Yushin G. Li-ion battery materials: Present and future. *Mater Today* 2015.
22 1185 <https://doi.org/10.1016/j.mattod.2014.10.040>.
23
24 1186 [82] Zuo X, Zhu J, Müller-Buschbaum P, Cheng YJ. Silicon based lithium-ion battery anodes: A
25 1187 chronicle perspective review. *Nano Energy* 2017. <https://doi.org/10.1016/j.nanoen.2016.11.013>.
26
27 1188 [83] Zhang WJ. A review of the electrochemical performance of alloy anodes for lithium-ion batteries.
28 1189 *J Power Sources* 2011. <https://doi.org/10.1016/j.jpowsour.2010.07.020>.
29
30 1190 [84] Wang H. TEM Study of Electrochemical Cycling-Induced Damage and Disorder in LiCoO₂
31 1191 Cathodes for Rechargeable Lithium Batteries. *J Electrochem Soc* 1999.
32 1192 <https://doi.org/10.1149/1.1391631>.
33
34 1193 [85] Qi Y, Harris SJ. In Situ Observation of Strains during Lithiation of a Graphite Electrode. *J*
35 1194 *Electrochem Soc* 2010. <https://doi.org/10.1149/1.3377130>.
36
37 1195 [86] Vetter J, Novák P, Wagner MR, Veit C, Möller KC, Besenhard JO, et al. Ageing mechanisms in
38 1196 lithium-ion batteries. *J Power Sources* 2005;147:269–81.
39 1197 <https://doi.org/10.1016/j.jpowsour.2005.01.006>.
40
41 1198 [87] Kabir M. and DDE. Degradation mechanisms in Li-ion batteries: a state-of-the-art review. *Int J*
42 1199 *Energy Res* 2017;41:1963–86. <https://doi.org/10.1002/er.3762>.
43
44 1200 [88] Rhodes K, Dudney N, Lara-Curzio E, Daniel C. Understanding the Degradation of Silicon
45 1201 Electrodes for Lithium-Ion Batteries Using Acoustic Emission. *J Electrochem Soc*
46 1202 2010;157:A1354. <https://doi.org/10.1149/1.3489374>.
47
48 1203 [89] Etienne A, Idrissi H, Roué L. On the decrepitation mechanism of MgNi and LaNi₅-based
49 1204 electrodes studied by in situ acoustic emission. *J Power Sources* 2011;196:5168–73.

- 1
2
3 1205 <https://doi.org/10.1016/j.jpowsour.2011.01.098>.
- 4
5 1206 [90] Etiemble A, Bernard P, Idrissi H, Roué L. New insights into the pulverization of LaNi₅-based
6 1207 alloys with different Co contents from electrochemical acoustic emission measurements.
7
8 1208 *Electrochim Acta* 2015;186:112–6. <https://doi.org/10.1016/j.electacta.2015.09.171>.
- 9
10 1209 [91] Inoue H, Tsuzuki R, Nohara S, Iwakura C. In Situ Monitoring of Hydrogen Storage Alloy
11 1210 Negative Electrode during Charging by an Acoustic Emission Technique. *Electrochem Solid-State*
12 1211 *Lett* 2006;9:A504. <https://doi.org/10.1149/1.2337864>.
- 14 1212 [92] Ohzuku T. Monitoring of Particle Fracture by Acoustic Emission during Charge and Discharge of
15 1213 LiMnO₂ Cells. *J Electrochem Soc* 1997;144:3496. <https://doi.org/10.1149/1.1838039>.
- 17 1214 [93] Kircheva N, Genies S, Chabrol C, Thivel PX. Evaluation of acoustic emission as a suitable tool for
18 1215 aging characterization of LiAl/LiMnO₂ cell. *Electrochim Acta* 2013;88:488–94.
19 1216 <https://doi.org/10.1016/j.electacta.2012.10.121>.
- 22 1217 [94] Tranchot A, Etiemble A, Thivel PX, Idrissi H, Roué L. In-situ acoustic emission study of Si-based
23 1218 electrodes for Li-ion batteries. *J Power Sources* 2015;279:259–66.
24 1219 <https://doi.org/10.1016/j.jpowsour.2014.12.126>.
- 25 1220 [95] Villevieille C, Boinet M, Monconduit L. Direct evidence of morphological changes in conversion
26 1221 type electrodes in Li-ion battery by acoustic emission. *Electrochem Commun* 2010;12:1336–9.
27 1222 <https://doi.org/10.1016/j.elecom.2010.07.014>.
- 28 1223 [96] Kircheva N, Genies S, Brun-Buisson D, Thivel P-X. Study of Solid Electrolyte Interface
29 1224 Formation and Lithium Intercalation in Li-Ion Batteries by Acoustic Emission. *J Electrochem Soc*
30 1225 2011. <https://doi.org/10.1149/2.045201jes>.
- 31 1226 [97] MATSUO T, UCHIDA M, CHO H. Development of Acoustic Emission Clustering Method to
32 1227 Detect Degradation of Lithium Ion Batteries. *J Solid Mech Mater Eng* 2011.
33 1228 <https://doi.org/10.1299/jmmp.5.678>.
- 34 1229 [98] Ohzuku T, Matoba N, Sawai K. Direct evidence on anomalous expansion of graphite-negative
35 1230 electrodes on first charge by dilatometry. *J Power Sources* 2001;97–98:73–7.
36 1231 [https://doi.org/10.1016/S0378-7753\(01\)00590-0](https://doi.org/10.1016/S0378-7753(01)00590-0).
- 37 1232 [99] Obrovac MN, Krause LJ. Reversible Cycling of Crystalline Silicon Powder. *J Electrochem Soc*
38 1233 2007. <https://doi.org/10.1149/1.2402112>.
- 39 1234 [100] Kalnaus S, Rhodes K, Daniel C. A study of lithium ion intercalation induced fracture of silicon
40 1235 particles used as anode material in Li-ion battery. *J Power Sources* 2011;196:8116–24.
41 1236 <https://doi.org/10.1016/j.jpowsour.2011.05.049>.
- 42 1237 [101] Schiele A, Breitung B, Mazilkin A, Schweidler S, Janek J, Gumbel S, et al. Silicon nanoparticles
43 1238 with a polymer-derived carbon shell for improved lithium-ion batteries: Investigation into volume

- 1
2
3 1239 expansion, gas evolution, and particle fracture. ACS Omega 2018.
4
5 1240 <https://doi.org/10.1021/acsomega.8b02541>.
- 6 1241 [102] Woodford WH, Carter WC, Chiang YM. Design criteria for electrochemical shock resistant
7
8 1242 battery electrodes. Energy Environ Sci 2012. <https://doi.org/10.1039/c2ee21874g>.
- 9 1243 [103] Woodford WH, Carter WC, Chiang Y-M. Design criteria for electrochemical shock resistant
10
11 1244 battery electrodes. Energy Environ Sci 2012;5:8014. <https://doi.org/10.1039/c2ee21874g>.
- 12 1245 [104] Didier-laurent S, Idrissi H, Rou L. In-situ study of the cracking of metal hydride electrodes by
13
14 1246 acoustic emission technique 2008;179:412–6. <https://doi.org/10.1016/j.jpowsour.2007.12.073>.
- 15 1247 [105] Barai P, Mukherjee PP. Mechano-Electrochemical Model for Acoustic Emission Characterization
16
17 1248 in Intercalation Electrodes. J Electrochem Soc 2014. <https://doi.org/10.1149/2.0201411jes>.
- 18 1249 [106] Komagata S, Kuwata N, Baskaran R, Kawamura J, Sato K, Mizusaki J. Detection of Degradation
19
20 1250 of Lithium-Ion Batteries with Acoustic Emission Technique. ECS Trans 2019.
21
22 1251 <https://doi.org/10.1149/1.3334804>.
- 23 1252 [107] Tang C, Yuan Z, Liu G, Jiang S, Hao W. Acoustic emission analysis of 18,650 lithium-ion battery
24
25 1253 under bending based on factor analysis and the fuzzy clustering method. Eng Fail Anal 2020.
26
27 1254 <https://doi.org/10.1016/j.engfailanal.2020.104800>.
- 28 1255 [108] Ladpli P, Liu C, Kopsaftopoulos F, Chang FK. Estimating Lithium-ion Battery State of Charge
29
30 1256 and Health with Ultrasonic Guided Waves Using an Efficient Matching Pursuit Technique. ITEC
31
32 1257 Asia-Pacific 2018 - 2018 IEEE Transp Electrif Conf Expo, Asia-Pacific E-Mobility A Journey
33 1258 from Now Beyond 2018. <https://doi.org/10.1109/ITEC-AP.2018.8433297>.
- 34 1259 [109] Hsieh AG, Bhadra S, Hertzberg BJ, Gjeltema PJ, Goy A, Fleischer JW, et al. Electrochemical-
35
36 1260 acoustic time of flight: In operando correlation of physical dynamics with battery charge and
37
38 1261 health. Energy Environ Sci 2015;8:1569–77. <https://doi.org/10.1039/c5ee00111k>.
- 39 1262 [110] Bhadra S, Hsieh AG, Wang MJ, Hertzberg BJ, Steingart DA. Anode Characterization in Zinc-
40
41 1263 Manganese Dioxide AA Alkaline Batteries Using Electrochemical-Acoustic Time-of-Flight
42
43 1264 Analysis. J Electrochem Soc 2016;163:A1050–6. <https://doi.org/10.1149/2.1201606jes>.
- 44 1265 [111] Chou YS, Hsu NY, Jeng KT, Chen KH, Yen SC. A novel ultrasonic velocity sensing approach to
45
46 1266 monitoring state of charge of vanadium redox flow battery. Appl Energy 2016;182:253–9.
47
48 1267 <https://doi.org/10.1016/j.apenergy.2016.08.125>.
- 49 1268 [112] Robinson JB, Maier M, Alster G, Compton T, Brett DJL, Shearing PR. Spatially resolved
50
51 1269 ultrasound diagnostics of Li-ion battery electrodes. Phys Chem Chem Phys 2019;21:6354–61.
52 1270 <https://doi.org/10.1039/c8cp07098a>.
- 53 1271 [113] Gold L, Bach T, Virsik W, Schmitt A, Müller J, Staab TEM, et al. Probing lithium-ion batteries'
54
55 1272 state-of-charge using ultrasonic transmission – Concept and laboratory testing. J Power Sources
- 56
57
58
59
60

- 1
2
3 1273 2017;343:536–44. <https://doi.org/10.1016/j.jpowsour.2017.01.090>.
- 4
5 1274 [114] Bauermann LP, Mesquita L., Bischoff C, Drews M, Fitz O, Heuer A, et al. Scanning acoustic
6 1275 microscopy as a non-destructive imaging tool to localize defects inside battery cells. *J Power*
7 1276 *Sources Adv* 2020. <https://doi.org/https://doi.org/10.1016/j.powera.2020.100035>.
- 8
9 1277 [115] Ladpli P, Kopsaftopoulos F, Nardari R, Chang F-K. Battery charge and health state monitoring via
10 1278 ultrasonic guided-wave-based methods using built-in piezoelectric transducers. *Smart Mater*
11 1279 *Nondestruct Eval Energy Syst* 2017 2017;10171:1017108. <https://doi.org/10.1117/12.2260107>.
- 12
13 1280 [116] Ladpli P, Kopsaftopoulos F, Chang FK. Estimating state of charge and health of lithium-ion
14 1281 batteries with guided waves using built-in piezoelectric sensors/actuators. *J Power Sources*
15 1282 2018;384:342–54. <https://doi.org/10.1016/j.jpowsour.2018.02.056>.
- 16
17 1283 [117] Popp H, Glanz G, Alten K, Gocheva I, Berghold W, Bergmann A. Mechanical frequency response
18 1284 analysis of lithium-ion batteries to disclose operational parameters. *Energies* 2018;11:1–13.
19 1285 <https://doi.org/10.3390/en11030541>.
- 20
21 1286 [118] Popp H, Koller M, Keller S, Glanz G, Klambauer R, Bergmann A. State Estimation Approach of
22 1287 Lithium-Ion Batteries by Simplified Ultrasonic Time-of-Flight Measurement. *IEEE Access*
23 1288 2019;7:170992–1000. <https://doi.org/10.1109/ACCESS.2019.2955556>.
- 24
25 1289 [119] Koyama Y, Chin TE, Rhyner U, Holman RK, Hall SR, Chiang YM. Harnessing the actuation
26 1290 potential of solid-state intercalation compounds. *Adv Funct Mater* 2006.
27 1291 <https://doi.org/10.1002/adfm.200500633>.
- 28
29 1292 [120] Reimers JN, Dahn JR. Electrochemical and In Situ X-Ray Diffraction Studies of Lithium
30 1293 Intercalation in Li_xCoO_2 . *J Electrochem Soc* 1992. <https://doi.org/10.1149/1.2221184>.
- 31
32 1294 [121] Knehr KW, Hodson T, Bommier C, Davies G, Kim A, Steingart DA. Understanding Full-Cell
33 1295 Evolution and Non-chemical Electrode Crosstalk of Li-Ion Batteries. *Joule* 2018;2:1146–59.
34 1296 <https://doi.org/10.1016/j.joule.2018.03.016>.
- 35
36 1297 [122] Tavassol H, Jones EMC, Sottos NR, Gewirth AA. Electrochemical stiffness in lithium-ion
37 1298 batteries. *Nat Mater* 2016;15:1182–7. <https://doi.org/10.1038/nmat4708>.
- 38
39 1299 [123] Sood B, Hendricks C, Osterman M, Pecht M. Health monitoring of lithium-ion batteries. *Electron*
40 1300 *Device Fail Anal* 2014;16:4–16. <https://doi.org/10.1109/ISPCE.2013.6664165>.
- 41
42 1301 [124] Pham MTM, Darst JJ, Finegan DP, Robinson JB, Heenan TMM, Kok MDR, et al. Correlative
43 1302 acoustic time-of-flight spectroscopy and X-ray imaging to investigate gas-induced delamination in
44 1303 lithium-ion pouch cells during thermal runaway. *J Power Sources* 2020.
45 1304 <https://doi.org/10.1016/j.jpowsour.2020.228039>.
- 46
47 1305 [125] Zappen H, Fuchs G, Gitis A, Sauer DU. In-operando impedance spectroscopy and ultrasonic
48 1306 measurements during high-temperature abuse experiments on lithium-ion batteries. *Batteries* 2020.

- 1
2
3 1307 <https://doi.org/10.3390/batteries6020025>.
- 4
5 1308 [126] Chang W, Bommier C, Fair T, Yeung J, Patil S, Steingart D. Understanding Adverse Effects of
6 1309 Temperature Shifts on Li-Ion Batteries : An Operando Acoustic Study Understanding Adverse
7 Effects of Temperature Shifts on Li-Ion Batteries : An Operando Acoustic Study 2020.
8 1310
9 1311 <https://doi.org/10.1149/1945-7111/ab6c56>.
- 10
11 1312 [127] Rodrigues M-TF, Babu G, Gullapalli H, Kalaga K, Sayed FN, Kato K, et al. A materials
12 1313 perspective on Li-ion batteries at extreme temperatures. *Nat Energy* 2017.
13
14 1314 <https://doi.org/10.1038/nenergy.2017.108>.
- 15
16 1315 [128] Bommier C, Lu Y, Williams M, Bommier C, Chang W, Lu Y, et al. In Operando Acoustic
17 1316 Detection of Lithium Metal Plating in Commercial LiCoO₂ / Graphite Pouch Cells. *Cell Reports*
18 1317 *Phys Sci* 2020:100035. <https://doi.org/10.1016/j.xcrp.2020.100035>.
- 19
20 1318 [129] Zang X, Yan L, Yang Y, Pan H, Nie Z, Jung KW, et al. Monitoring the State-of-Charge of a
21 1319 Vanadium Redox Flow Battery with the Acoustic Attenuation Coefficient: An In Operando
22 Noninvasive Method. *Small Methods* 2019;3:1–9. <https://doi.org/10.1002/smt.201900494>.
- 23
24 1320
25 1321 [130] Stumper J, Stone C. Recent advances in fuel cell technology at Ballard. *J Power Sources* 2008.
26 1322 <https://doi.org/10.1016/j.jpowsour.2007.08.071>.
- 27
28 1323 [131] Voss HH, Wilkinson DP, Pickup PG, Johnson MC, Basura V. Anode water removal: A water
29 1324 management and diagnostic technique for solid polymer fuel cells. *Electrochim Acta* 1995.
30 1325 [https://doi.org/10.1016/0013-4686\(94\)00266-4](https://doi.org/10.1016/0013-4686(94)00266-4).
- 31
32 1326 [132] Bethapudi VS, Hack J, Trogadas P, Hinds G, Shearing PR, Brett DJL, et al. Hydration state
33 1327 diagnosis in fractal flow-field based polymer electrolyte membrane fuel cells using acoustic
34 1328 emission analysis. *Energy Convers Manag* 2020;220:113083.
35 1329 <https://doi.org/10.1016/j.enconman.2020.113083>.
- 36
37 1330 [133] Hinaje M, Sadli I, Martin JP, Thounthong P, Raël S, Davat B. Online humidification diagnosis of
38 1331 a PEMFC using a static DC-DC converter. *Int J Hydrogen Energy* 2009.
39 1332 <https://doi.org/10.1016/j.ijhydene.2009.01.076>.
- 40
41 1333 [134] Rubatat L, Rollet AL, Gebel G, Diat O. Evidence of elongated polymeric aggregates in Nafion.
42 1334 *Macromolecules* 2002. <https://doi.org/10.1021/ma011578b>.
- 43
44 1335 [135] Tang Y, Yuan W, Pan M, Li Z, Chen G, Li Y. Experimental investigation of dynamic performance
45 1336 and transient responses of a kW-class PEM fuel cell stack under various load changes. *Appl*
46 1337 *Energy* 2010;87:1410–7. <https://doi.org/10.1016/J.APENERGY.2009.08.047>.
- 47
48 1338 [136] Legros B, Thivel P-X, Bultel Y, Boinet M, Nogueira RP. Electrochemical Impedance and
49 1339 Acoustic Emission Survey of Water Desorption in Nafion Membranes. *Electrochem Solid-State*
50 1340 *Lett* 2009;12:B116. <https://doi.org/10.1149/1.3131728>.
- 51
52
53
54
55
56
57
58
59
60

- 1
2
3 1341 [137] Bethapudi VS, Hack J, Trogadas P, Hinds G, Shearing PR, Brett DJL, et al. Hydration state
4 1342 diagnosis in fractal flow-field based polymer electrolyte membrane fuel cells using acoustic
5 1343 emission analysis. *Energy Convers Manag* 2020. <https://doi.org/10.1016/j.enconman.2020.113083>.
6
7 1344 [138] Dev B, Walter ME, Arkenberg GB, Swartz SL. Mechanical and thermal characterization of a
8 1345 ceramic/glass composite seal for solid oxide fuel cells. *J Power Sources* 2014;245:958–66.
9 1346 <https://doi.org/10.1016/j.jpowsour.2013.07.054>.
10
11 1347 [139] Malzbender J, Steinbrech RW. Advanced measurement techniques to characterize thermo-
12 1348 mechanical aspects of solid oxide fuel cells. *J Power Sources* 2007.
13 1349 <https://doi.org/10.1016/j.jpowsour.2007.07.072>.
14
15 1350 [140] Sato K, Omura H, Hashida T, Yashiro K, Yugami H, Kawada T, et al. Tracking the onset of
16 1351 damage mechanism in ceria-based solid oxide fuel cells under simulated operating conditions. *J*
17 1352 *Test Eval* 2006.
18
19 1353 [141] Sato K, Hashida T, Yashiro K, Yugami H, Kawada T, Mizusaki J. Mechanical damage evaluation
20 1354 of solid oxide fuel cells under simulated operating conditions. *J Ceram Soc Japan* 2005;113:562–4.
21 1355 <https://doi.org/10.2109/jcersj.113.562>.
22
23 1356 [142] Rangel-Hernández VH, Fang Q, Babelot C, Lohoff R, Blum L. An experimental investigation of
24 1357 fracture processes in glass-ceramic sealant by means of acoustic emission. *Int J Hydrogen Energy*
25 1358 2020. <https://doi.org/10.1016/j.ijhydene.2020.07.031>.
26
27 1359 [143] Kumada K, Sato K, Hashida T. Evaluation of Mechanical Damages in SOFCs during Start/Stop
28 1360 Operation by Using Acoustic Emission Technique. *ECS Trans* 2017.
29 1361 <https://doi.org/10.1149/07801.2355ecst>.
30
31 1362 [144] Crowther TG, Wade AP, Wentzell PD, Gopal R. Characterization of acoustic emission from an
32 1363 electrolysis cell. *Anal Chim Acta* 1991. [https://doi.org/10.1016/0003-2670\(91\)90030-9](https://doi.org/10.1016/0003-2670(91)90030-9).
33
34 1364 [145] Maier M, Meyer Q, Majasan J, Tan C, Dedigama I, Robinson J, et al. Operando flow regime
35 1365 diagnosis using acoustic emission in a polymer electrolyte membrane water electrolyser. *J Power*
36 1366 *Sources* 2019;424:138–49. <https://doi.org/10.1016/j.jpowsour.2019.03.061>.
37
38 1367 [146] Maier M, Meyer Q, Majasan J, Owen RE, Robinson JB, Dodwell J, et al. Diagnosing Stagnant Gas
39 1368 Bubbles in a Polymer Electrolyte Membrane Water Electrolyser Using Acoustic Emission. *Front*
40 1369 *Energy Res* 2020;8. <https://doi.org/10.3389/fenrg.2020.582919>.
41
42 1370 [147] Maier M, Owen RE, Pham MTM, Dodwell J, Majasan J, Robinson JB, et al. Acoustic time-of-
43 1371 flight imaging of polymer electrolyte membrane water electrolyzers to probe internal structure and
44 1372 flow characteristics. *Int J Hydrogen Energy* 2021. <https://doi.org/10.1016/j.ijhydene.2021.01.077>.
45
46 1373 [148] Robinson J, Xi K, Kumar RV, Ferrari AC, Au H, Titirici M-M, et al. 2021 Roadmap on Lithium
47 1374 Sulfur Batteries. *J Phys Energy* 2021;2:0–31.

- 1
2
3 1375 [149] Kundu S, Fowler MW, Simon LC, Grot S. Morphological features (defects) in fuel cell membrane
4 1376 electrode assemblies. *J Power Sources* 2006;157:650–6.
5
6 1377 <https://doi.org/https://doi.org/10.1016/j.jpowsour.2005.12.027>.
7
8 1378 [150] Obeisun OA, Finegan DP, Engebretsen E, Robinson JB, Taiwo OO, Hinds G, et al. Ex-situ
9 1379 characterisation of water droplet dynamics on the surface of a fuel cell gas diffusion layer through
10 1380 wettability analysis and thermal characterisation. *Int J Hydrogen Energy* 2017;42.
11 1381 <https://doi.org/10.1016/j.ijhydene.2017.01.003>.
12
13 1382 [151] Singh Y, White RT, Najm M, Haddow T, Pan V, Orfino FP, et al. Tracking the evolution of
14 1383 mechanical degradation in fuel cell membranes using 4D in situ visualization. *J Power Sources*
15 1384 2019;412:224–37. <https://doi.org/https://doi.org/10.1016/j.jpowsour.2018.11.049>.
16
17 1385 [152] Tawfik H, Hung Y, Mahajan D. Metal bipolar plates for PEM fuel cell—A review. *J Power*
18 1386 *Sources* 2007;163:755–67. <https://doi.org/https://doi.org/10.1016/j.jpowsour.2006.09.088>.
19
20 1387 [153] Dhakate SR, Mathur RB, Kakati BK, Dhami TL. Properties of graphite-composite bipolar plate
21 1388 prepared by compression molding technique for PEM fuel cell. *Int J Hydrogen Energy*
22 1389 2007;32:4537–43. <https://doi.org/https://doi.org/10.1016/j.ijhydene.2007.02.017>.
23
24 1390 [154] Kim YS, Pivovar BS. The Membrane–Electrode Interface in PEFCs. *J Electrochem Soc*
25 1391 2010;157:B1616. <https://doi.org/10.1149/1.3481581>.
26
27 1392 [155] Wu Z, Wang S, Zhang L, Hu SJ. An analytical model and parametric study of electrical contact
28 1393 resistance in proton exchange membrane fuel cells. *J Power Sources* 2009;189:1066–73.
29 1394 <https://doi.org/https://doi.org/10.1016/j.jpowsour.2008.12.129>.
30
31 1395 [156] Mérida W, Harrington DA, Le Canut JM, McLean G. Characterisation of proton exchange
32 1396 membrane fuel cell (PEMFC) failures via electrochemical impedance spectroscopy. *J Power*
33 1397 *Sources* 2006;161:264–74. <https://doi.org/https://doi.org/10.1016/j.jpowsour.2006.03.067>.
34
35 1398 [157] Husar A, Serra M, Kunusch C. Description of gasket failure in a 7 cell PEMFC stack. *J Power*
36 1399 *Sources* 2007;169:85–91. <https://doi.org/https://doi.org/10.1016/j.jpowsour.2007.01.078>.
37
38 1400 [158] Stucki S, Scherer GG, Schlagowski S, Fischer E. PEM water electrolyzers: Evidence for
39 1401 membrane failure in 100 kW demonstration plants. *J Appl Electrochem* 1998;28:1041–9.
40 1402 <https://doi.org/10.1023/A:1003477305336>.
41
42 1403 [159] Lin R, Li B, Hou YP, Ma JM. Investigation of dynamic driving cycle effect on performance
43 1404 degradation and micro-structure change of PEM fuel cell. *Int J Hydrogen Energy* 2009;34:2369–
44 1405 76. <https://doi.org/https://doi.org/10.1016/j.ijhydene.2008.10.054>.
45
46 1406 [160] Flimban SGA, Hassan SHA, Rahman MM, Oh S-E. The effect of Nafion membrane fouling on the
47 1407 power generation of a microbial fuel cell. *Int J Hydrogen Energy* 2020;45:13643–51.
48 1408 <https://doi.org/https://doi.org/10.1016/j.ijhydene.2018.02.097>.
49
50
51
52
53
54
55
56
57
58
59
60

- 1
2
3 1409 [161] Stanic V, Hoberecht M. Mechanism of pinhole formation in membrane electrode assemblies for
4 1410 PEM fuel cells. Proc - Electrochem Soc 2004;PV 2004-21:391–401.
5
6 1411 <https://doi.org/10.1149/200421.0391PV>.
7
8 1412 [162] Mehta V, Cooper JS. Review and analysis of PEM fuel cell design and manufacturing. J Power
9 1413 Sources 2003;114:32–53. [https://doi.org/https://doi.org/10.1016/S0378-7753\(02\)00542-6](https://doi.org/https://doi.org/10.1016/S0378-7753(02)00542-6).
10
11 1414
12
13 1415
14 1416
15
16 1417
17 1418
18
19 1419
20
21 1420
22
23
24
25
26
27
28
29
30
31
32
33
34
35
36
37
38
39
40
41
42
43
44
45
46
47
48
49
50
51
52
53
54
55
56
57
58
59
60